A V0-ATPase-dependent apical trafficking pathway maintains the polarity of the intestinal absorptive membrane

Aurélien Bidaud-Meynard[1], Ophélie Nicolle[1], Markus Heck[1] and Grégoire Michaux[1, *]

Univ Rennes, CNRS, IGDR (Institut de Génétique et Développement de Rennes) - UMR 6290, F-35000 Rennes, France

* lead contact gmichaux@univ-rennes1.fr

8

9 **Summary statement**

10 V0-ATPase controls a late apical trafficking step involved in the maintenance of the apical
11 absorptive intestinal membrane and its depletion phenocopies the trafficking and structural
12 defects of MVID in *C. elegans*.

13

Abstract

Intestine function relies on the strong polarity of intestinal epithelial cells and the array of microvilli forming a brush border at their luminal pole. Combining genetic RNAi screen and *in vivo* super-resolution imaging in the *C. elegans* intestine, we uncovered that the V0 sector of the V-ATPase (V0-ATPase) controls a late apical trafficking step, involving RAB-11 endosomes and the SNARE SNAP-29, necessary to maintain the polarized localization of both apical polarity modules and brush border proteins. We show that the V0-ATPase pathway also genetically interacts with glycosphingolipids in enterocyte polarity maintenance. Finally, we demonstrate that depletion of the V0-ATPase fully recapitulates the severe structural, polarity and trafficking defects observed in enterocytes from patients with Microvillus inclusion disease (MVID) and used this new *in vivo* MVID model to follow the dynamics of microvillus inclusions. Hence, we describe a new function for the V0-ATPase in apical trafficking and epithelial polarity maintenance and the promising use of *C. elegans* intestine as an *in vivo* model to better understand the molecular mechanisms of rare genetic enteropathies.

29

30 ## Introduction

31 Considering that almost all nutrients in the diet are absorbed into blood across the
32 epithelial layer forming the small and large intestinal mucosa (Kiela and Ghishan, 2016),
33 proper establishment and maintenance of both the strong polarity of enterocytes and the array
34 of microvilli forming an absorptive brush border at their apical plasma membrane (PM) are
35 essential to ensure intestinal functions. In most species, including *C. elegans*, epithelial cell
36 polarity is achieved by actin and microtubule cytoskeleton reorganization, trafficking and
37 signalling-mediated polarized targeting of the CDC-42/PAR-3/PAR-6/PKC-3 (CDC-42/PAR)
38 and Crumbs/PALS1/Patj (CRB) modules at the apical pole and the Dlg/Scribble/Lgl (SCRIB)
39 module at the basolateral pole as well as domain-specific lipid distribution (Rodriguez-
40 Boulan and Macara, 2014). Particularly, CDC-42 has been shown to be a major player of
41 polarity maintenance by controlling the apical localization of PAR module components in *C.*
42 *elegans* intestine (Shafaq-Zadah et al., 2012) and MDCK cysts (Martin-Belmonte et al.,
43 2007). The establishment of the brush border, an extended PM surface for efficient nutrient
44 uptake, is thought to be highly dependent on actin cytoskeleton regulating factors which
45 create the force necessary for the onset and maintenance of the microvilli (Heintzelman and
46 Mooseker, 1990a, Heintzelman and Mooseker, 1990b, Crawley et al., 2014, Saegusa et al.,
47 2014).

48 Polarity establishment and brush border formation are early events in intestine
49 development that both rely on related cytoskeletal and trafficking pathways. In *C. elegans*,
50 Clathrin and AP-1 (Shafaq-Zadah et al., 2012, Zhang et al., 2012), glycosphingolipids (GSLs)
51 (Zhang et al., 2011), and the kinase Lats/WTS-1 (Kang et al., 2009) have been shown to play
52 a major role in the sorting of polarity modules and luminogenesis. In mammalian intestine
53 cellular models, the trafficking proteins Annexin 2, STX3, Rab8a and Rab11a, the actin

54 binding proteins Drebin E, Myosin 6 and Myosin 5 have been involved in the polarized
55 localization of PM transporters and brush border integrity (Hegan et al., 2012, Vogel et al.,
56 2015, Vacca et al., 2014, Hein et al., 2011) while the latter has been also involved in the
57 apical confinement of the PAR polarity module (Michaux et al., 2016).

58 Particularly, these studies highlighted the central role of RAB-11-dependent apical
59 trafficking in polarity maintenance and lumen integrity. Indeed, studies in MDCK cells
60 demonstrated the critical function of RAB-11^{+} endosomes in apical PM and lumen generation
61 by mediating PAR-3 targeting and Cdc42 activation through the exocyst complex (Colombie
62 et al., 2017, Bryant et al., 2010) as well as the adverse effect of dominant-negative Rab11
63 (Rab11^{DN}) expression on the apical localization of phospho-ezrin and E-Cadherin
64 (Desclozeaux et al., 2008). Furthermore, expression of Rab-11^{DN} or depletion of the Rab11^{+}
65 endosomes-associated motor Myosin 5B (Myo5B) decreased both ezrin phosphorylation at
66 the apical PM and microvilli size in intestinal cells model (Dhekne et al., 2014), and these
67 polarity and structural consequences were confirmed in Rab11a intestinal-specific knock out
68 mice model (Sobajima et al., 2014). Finally, defective RAB-11-dependent trafficking has
69 been associated with congenital enteropathies, which are characterized by polarity and brush
70 border structural defects (Vogel et al., 2017a). However, little is known about the relationship
71 between polarity modules, brush border and apical trafficking components and their
72 sequential involvement in establishing and maintaining an absorptive intestinal apical PM,
73 especially *in vivo*.

74 *C. elegans* intestine is composed of 20 polarized enterocytes similar to that of
75 mammalian cells and the nematode embryonic and larval stages have been widely used to
76 understand polarity and lumen establishment and maintenance, respectively (McGhee, 2007).
77 By performing an RNAi screen to target a library of trafficking and cytoskeleton factors in *C.*
78 *elegans* larvae, we unveiled that the depletion of the V0 sector of the vacuolar-ATPase (V-

79 ATPase) induces a cytoplasmic and basolateral mislocalization of both PAR polarity module
80 and brush border components. The V-ATPase is a large hetero-multimeric complex (20
81 subunits in *C. elegans, vha-1* to *vha-18*, *spe-5* and *unc-32*), organized in two main sectors: a
82 V1 sector responsible for ATP hydrolysis which provides the energy to the V0 sector, which
83 transports protons (Lee et al., 2010). The whole V-ATPase complex is responsible for the
84 acidification of intracellular compartments, such as endosomes or lysosomes and plays a
85 major role in PM proteins trafficking (Maxson and Grinstein, 2014), while its V0
86 transmembrane sector (V0-ATPase) has been implicated in the fusion to the yeast vacuole
87 (Baars et al., 2007) as well as that of synaptic vesicles in drosophila and humans (Hiesinger et
88 al., 2005, Di Giovanni et al., 2010), in an acidification-independent manner. In *C. elegans*,
89 the V0-ATPase subunits *vha-5*, *vha-6* and *vha-19* are required for exosome containing vesicle
90 apical exocytosis in the epidermis (Liegeois et al., 2006), intestinal lumen pH regulation
91 (Allman et al., 2009) and RME-2 receptor trafficking in oocytes (Knight et al., 2012) but no
92 role in polarity maintenance has been assigned to this complex before.

93 Here, we show that interfering with the V0-ATPase-mediated polarity maintenance
94 mechanism in *C. elegans* fully recapitulates the polarity, trafficking and structural phenotypes
95 observed in patients suffering from Microvillus inclusion disease (MVID, OMIM: 251850).
96 MVID is caused by mutations in the genes coding for myosin-5B (MYO5B) (Muller et al.,
97 2008), syntaxin-3 (STX3) (Wiegerinck et al., 2014) or Munc18-2/STXBP-2 (STXBP2)
98 (Vogel et al., 2017b), three proteins regulating apical trafficking. The major hallmarks of this
99 disease are a microvillus atrophy, the rare formation of microvillus inclusions, as well as a
100 loss of subapical RAB-11^{+} endosomes (Schneeberger et al., 2018). Hence, we propose that
101 the V0-ATPase is essential to control apical trafficking and polarity maintenance.

102

102

103 ## Results

104 **V0-ATPase depletion affects the polarity of brush border and polarity components in**
105 **the *C. elegans* intestine**

106 To identify new common regulators of polarity and brush border maintenance *in vivo*,
107 we performed a two-step RNAi screen targeting 408 genes essential for survival, conserved
108 in humans and implicated in membrane trafficking and cytoskeleton regulation. First, we
109 examined the effect of their silencing on the localization of the polarity module component
110 CDC-42 at the apical PM of enterocytes of *C. elegans* larvae. We then performed a secondary
111 screen to evaluate the ability of the hits decreasing CDC-42 apical localization to also disturb
112 the polarity of the brush border specific actin cross-linker ERM-1 (Table S1 and Fig S1A).
113 This systematic RNAi screen first confirmed the involvement of clathrin (*chc-1*), AP-1 (*aps-*
114 *1*) and GSLs biosynthesis enzymes (i.e. *sptl-1*, *fasn-1*, *pod-2*) (Zhang et al., 2012, Shafaq-
115 Zadah et al., 2012, Zhang et al., 2011) in the maintenance of intestinal polarity (Table S1)
116 and identified several genes belonging to the biosynthetic and endocytic pathways, as well as
117 10 subunits of the V-ATPase complex, a major player of intracellular trafficking by
118 regulating endosomal acidification (Table S1). This screen performed using overexpressed
119 markers, was then confirmed by silencing several subunits of the V-ATPase complex and
120 studying the endogenous localization of genome-edited mNeongreen or GFP-tagged ERM-1
121 as well as the polarity module components PAR-6 and PKC-3. Consistently, knockdown of
122 all the V-ATPase complex subunits decreased by 15-40% the apical/cytoplasmic ratio of the
123 PAR module proteins and of ERM-1 (Fig 1A-F). This indicates that a V-ATPase
124 acidification-dependent mechanism is involved in the apical confinement of brush border and
125 polarity module components. Intriguingly, depletion of the subunits *vha-1*, *-4* and *-19*,
126 belonging to the V0-ATPase, also induced a basolateral localization of ERM-1, while no

127 basolateral mislocalization was observed upon silencing of the V1-ATPase subunits *vha-8*,
128 which has been shown to inhibit V-ATPase-dependent acidification (Ji et al., 2006) and *vha-*
129 *15* (Fig 1A, G). Furthermore, endogenous PAR-6 and PKC-3 could also be specifically
130 observed at the basolateral PM in ~20% of the worms upon V0-ATPase subunits depletion
131 (Fig 1B). To evaluate if V0-ATPase silencing induces a global polarity inversion of the
132 enterocytes we studied the effect of the silencing of the V0-ATPase subunit *vha-1*, which
133 destabilizes the whole V0-ATPase sector (Fig S1 B-C) on the polarized localization of the
134 apical peptide transporter PEPT-1 (OPT-2) and the P-glycoprotein PGP-1 as well as the
135 basolateral pyruvate transporter SLCF-1. Notably, silencing of *vha-1* did not induce a
136 significant effect on the cortical confinement of those highly polarized proteins and none of
137 them accumulated at the contralateral PM (Fig 1H-K and Fig S2A), supporting the notion that
138 the enterocyte polarity is only partially compromised upon V0-ATPase depletion. Overall,
139 these data indicate that the V0-ATPase sector specifically controls the polarized localization
140 of both brush border (ERM-1) and polarity module components (PAR-6, PKC-3) in
141 enterocytes.
142
143 **V0-ATPase depletion specifically affects the apical recycling pathway**
144 The V-ATPase complex controls the acidification of various endosomes along the
145 biosynthetic and endocytic-recycling routes (Forgac, 2007). Using Transmission Electron
146 Microscopy (TEM), we observed the presence of abnormal large organelles (0.1–0.3 μm in
147 diameter with variable electron density and heterogeneous content) with features of vesicles
148 and lysosomes upon inhibition of both V0 and V1-ATPase subunits (Fig 2A-B). These
149 "mixed" organelles have been already described in the *C. elegans* epidermis and in
150 mammalian cells upon V0-/V1-ATPase silencing or chemical inhibition of the V-ATPase
151 complex function, and have been proposed to affect protein sorting along the secretory and

152 lysosomal pathways (Sobota et al., 2009, Liegeois et al., 2006), probably due to an endosome
153 acidification failure. The presence of mixed organelles was confirmed by the accumulation of
154 several endosomal markers in large cytoplasmic structures, such as LMP-1 (lysosomes),
155 RAB-7 (late endosomes) and RAB-10 (basolateral recycling endosomes) (Fig 2C and S2B),
156 upon both V0-and V1-ATPase silencing.

157 Strikingly, V0- but not V1-ATPase depletion led to the specific accumulation of
158 electron-lucent vesicular structures in the cytoplasm (Fig 2D), which were reminiscent of an
159 apical trafficking defect. The number of RAB-5^{+} endosomes was slightly decreased upon
160 both V0 and V1-ATPase silencing (Fig 2E-F). However, RAB-11 endosomes virtually
161 disappeared from the apical PM and accumulated in the cytoplasm upon V0- but not V1-
162 ATPase knockdown (Fig 2G-H). Considering that *rab-11* knockdown also induced a
163 basolateral mislocalization of ERM-1 (Fig 2I-J), similarly to *vha-1(RNAi)* (Fig 1B, G) this
164 indicates that V0-ATPase controls the enterocyte polarity by regulating a late trafficking step
165 through RAB-11^{+} endosomes.

166

167 **SNAP-29 is involved in V0-ATPase-mediated polarity maintenance**

168 To identify other molecular components of this V0-ATPase-mediated control of
169 intestinal polarity beyond the interaction with RAB-11, the effect of V0- or V1-ATPase
170 depletion was assayed on several soluble trafficking factors with a highly polarized
171 localization. The PM localization of CHC-1/clathrin and the syntaxin UNC-64 (the
172 presumptive mammalian STX3 ortholog) was strongly decreased and increased, respectively
173 (Fig 3 A-B) while that of the syntaxin SYX-1 (SYN-1) was only slightly decreased (Fig S2C)
174 upon all V-ATPase complex subunits depletion, suggesting a trafficking defect, but no sector-
175 specificity. Strikingly, *vha-1/V0-ATPase(RNAi)* specifically decreased the apical localization
176 of the soluble N-ethylmaleimide-sensitive factor-attachment protein receptors (SNAREs)

177 component SNAP-29, while *vha-8/V1-ATPase(RNAi)* did not (Fig 3C). SNAP-29 belongs to
178 the SNAP23/25/29 family of SNARE proteins that interact with syntaxins and sec/munc
179 proteins to promote vesicle fusion (Sudhof and Rothman, 2009). Its depletion has been shown
180 to affect the morphology of various organelles, including recycling endosomes, and
181 consequently endocytosis, secretion as well as autophagy pathways in *C. elegans* intestine
182 (Sato et al., 2011, Guo et al., 2014). To test whether SNAP-29 is involved in polarity
183 maintenance, *snap-29* was silenced by RNAi (Fig S2 D-E) and the PM localization of ERM-1
184 was assessed. *snap-29* silencing induced a basolateral mislocalization of ERM-1 (Bl/cyto
185 ratio >1.5) in 44.3% of the worms whereas only 20.8% of control (L4440) worms displayed a
186 ratio >1.5 (Fig 3D-E). Finally, the effect of *snap-29(RNAi)* was assayed on a strain co-
187 expressing RAB-11::GFP and the V0-ATPase subunit VHA-6::mCh. While *snap-29*
188 knockdown also induced a dramatic loss of RAB-11 signal, it did not affect that of V0-
189 ATPase (Fig 3 F-G). Hence, these data strongly suggest that SNAP-29 acts downstream of
190 the V0-ATPase to maintain the enterocyte polarity.
191
192 **High-resolution map of the apical PM revealed that V0-ATPase localizes to microvilli**
193 The V0-ATPase has been localized at the apical PM of intestinal epithelia in *C.*
194 *elegans* (Zhu et al., 2015) and proposed to traffic to the brush border in Caco-2 cells (Collaco
195 et al., 2013). However, conventional confocal imaging in *C. elegans* only allowed to
196 determine the apical polarity of markers, but not their precise position regarding the apical
197 PM (e.g. microvilli, terminal web, subapical). The precise localization of the V0-ATPase as
198 well as that of some of the above-mentioned polarity markers was thus assessed by live
199 super-resolution confocal microscopy. This technique confirmed that ERM-1 accumulates in
200 the microvilli, while ACT-5, PGP-1 and SNAP-29 were present at both the microvilli and the
201 underlying terminal web (Fig 4A-B). SNAP-29 has been previously shown to localize on

202 RAB-11^{+} endosomes in *C. elegans* intestine (Kang et al., 2011), and this interaction seems to
203 take place at the presumptive terminal web level, where the PAR component PKC-3 mostly
204 accumulates (Fig 4A-D). Finally, the V0-ATPase subunit VHA-6 was localized to the
205 microvilli, above the RAB-11 apical staining (Fig 4D). Overall, these results strongly suggest
206 that the V0-ATPase localizes at microvilli from where it controls the apical localization of
207 brush border and polarity modules by regulating a late trafficking step through RAB-11^{+}
208 endosomes in a SNAP-29-dependent manner.
209

210 **V0-ATPase interacts with GSLs but not with AP-1 in intestinal polarity maintenance**

211 Interestingly, two trafficking and possibly cooperating pathways have been invoked
212 as major regulators of intestinal polarity maintenance in *C. elegans*: GSLs and
213 Clathrin/Clathrin adaptor AP-1. Particularly, depletion of the AP-1 complex subunit *aps-1* or
214 of enzymes along the GSLs biosynthetic pathway (i.e. *let-767*, *acs-1*, *pod-2* or *sptl-1*) has
215 been shown to induce the contralateral PM localization of polarized proteins and a loss of
216 RAB-11 endosomes, similarly to *vha-1* depletion (Shafaq-Zadah et al., 2012, Zhang et al.,
217 2012, Zhang et al., 2011). First, to test the putative genetic interaction between the V0-
218 ATPase and the GSLs and AP-1 pathways, *vha-1* and *aps-1* were co-depleted by RNAi and
219 *vha-1* was depleted in a *let-767(s2176)* loss-of-function mutant balanced with the *sDp3*
220 duplication (Zhang et al., 2012). The single depletion of *vha-1* and *aps-1* induced a 56% and
221 50% increase of ERM-1 Bl/cytoplasmic ratio, respectively, and the co-depletion of these
222 factors led to a 109% increase of this ratio, suggesting an additive effect (Fig 5A).
223 Conversely, while the Bl/cyto ratio of ERM-1 in the balanced *let-767(s2176)* mutant was not
224 different from control worms (ratio of 1.6 vs 1.5, respectively), this ratio was dramatically
225 increased upon *vha-1(RNAi)* co-depletion compared to control (ratio of 4.1; 2.9-fold increase)
226 or *vha-1(RNAi)* alone (ratio of 2.3; 1.7-fold increase) (Fig 5B-C). These results indicated that

227 V0-ATPase genetically interacts with GSLs, but not with AP-1 in intestinal polarity
228 maintenance.
229
230 **V0-ATPase depletion phenocopies Microvillus inclusion disease**
231 Next, we asked whether the polarity defects associated with V0-ATPase depletion
232 were associated with brush border structural defects. Combined TEM and super-resolution
233 imaging demonstrated that prolonged V0-ATPase depletion (72 and 96h of *vha-1(RNAi)*)
234 specifically induced a microvillus atrophy, with smaller, thinner or even absent microvilli at
235 the apical PM of enterocytes (Fig 6A-C). Conversely, V1-ATPase depletion (*vha-8(RNAi)*),
236 despite inducing a decreased worm size and a mild decrease of microvilli length, did not
237 affect the microvilli structure and organization (Figs 6A-C and S3A). The severe apical PM
238 defect induced by V0-ATPase depletion was observed along the whole surface of the
239 deformed lumen and was often associated with a local unhooking of microvilli membrane
240 from the underlying cytoskeleton (Fig S3B) as well as slightly lengthened adherens junctions
241 (CeAJs) (Fig S3C-D). Thus, V0-ATPase depletion specifically leads to severe apical PM
242 structural defects, which may affect the absorptive function of the enterocytes, in line with
243 the luminal accumulation of cellular or bacterial debris and the absence of yolk storage
244 granules observed in *vha-1(RNA)* but not *vha-8(RNAi)* worms (Fig S3E-F). In addition to
245 these apical PM defects, super-resolution microscopy showed that the brush border
246 components ACT-5 and ERM-1 adopt a pattern reminiscent of microvilli when mislocalized
247 to the basolateral PM (Fig 6D-E) although TEM analysis did not reveal the presence of *bona*
248 *fide* microvilli.
249 Surprisingly, prolonged V0-ATPase depletion led to the accumulation of rounded
250 ERM-1^{+} and ACT-5^{+} structures (Fig 7A-B), which displayed a microvilli-like pattern on
251 higher magnification (Fig 7C) and closely resemble cytoplasmic microvillus inclusions

252 (MVIs) observed in MVID patients (Iancu et al., 2007) and in *STXBP2* KO organoids MVID
253 model (Mosa et al., 2018). These structures are also enriched in PKC-3 and SNAP-29 (Fig
254 7D-E). TEM experiments performed on *vha-1* depleted worms confirmed the presence of
255 typical MVIs lined by inward-pointing microvilli (Fig 7F). We also observed many vacuole-
256 like structures with a wide size (0.1–0.6 μm in diameter), shape and electron-density
257 heterogeneity and containing cellular material (Fig 7G). These vacuole-like structures were
258 positive for the microvilli-specific activated phospho-form of ezrin, as observed by immuno-
259 EM (Fig 7H) and are similar to the already described "irregular" MVIs that are probably
260 immature or degrading MVIs (Iancu et al., 2007, Mosa et al., 2018). Strikingly, microvillus
261 atrophy and MVIs are cellular hallmarks of Microvillus inclusion disease (MVID, OMIM:
262 251850), a congenital disorder of intestinal epithelial cells (Ruemmele et al., 2006) caused by
263 mutations in the genes coding for the trafficking proteins Myosin 5B (MYO5B) (Muller et
264 al., 2008), Syntaxin3 (STX3) (Wiegerinck et al., 2014) or Munc18-2 (STXBP2) (Vogel et al.,
265 2017b). Interestingly, enterocytes of patients with MVID also displayed similar polarity
266 defects than that observed upon *vha-1(RNAi)*, such as the basolateral appearance of
267 microvilli-specific proteins (Wiegerinck et al., 2014), the basolateral mislocalization of PAR
268 polarity module components (Michaux et al., 2016) as well as the cytoplasmic displacement
269 of trafficking (i.e. STX3, the SNAREs family component SNAP23 and cellubrevin) (Dhekne
270 et al., 2018) proteins. Finally, MVID has also been associated with enlarged lysosomes
271 displaying a heterogeneous content (Fig 2A, C) and with the accumulation of cytoplasmic
272 translucent vesicles (Fig 2D) (Iancu et al., 2007, Vogel et al., 2016) as well as the specific
273 disorganization of Rab11^{+} apical recycling endosomes (Fig 2G-H) (Vogel et al., 2017a,
274 Talmon et al., 2012). Together with the fact that *snap-29(RNAi)* also induces polarity defects
275 (Fig 3D-G) and the formation of MVIs (Fig 7I), these observations strongly suggest that V0-
276 ATPase depletion in *C. elegans* fully recapitulates the defects observed in the enterocytes of

277 patients suffering from MVID and MVID *in vitro* mammalian models (Table S2, S3) (Mosa
278 et al., 2018).
279
280 **Study of MVIs dynamics in *C. elegans* model**
281 Using live microscopy in intestinal organoids derived from *STXBP2* knock-out mouse, we
282 recently contributed to show that MVIs can arise *de novo* in the cytoplasm or by
283 internalization of both the apical and the basolateral PM (Mosa et al., 2018). To test whether
284 these various modes of MVI onset are conserved in *C. elegans* upon V0-ATPase depletion,
285 we performed live imaging on endogenously expressed ERM-1::mNG after 96h of *vha-*
286 *1(RNAi)*. This experiment confirmed that MVI-like structures can rapidly nucleate in the
287 cytoplasm (~3 min) and remained in the cytoplasm from less than 3 min to more than 1h (Fig
288 8A and Movie S1-S2), a process that may involve lysosomal remodelling (Mosa et al., 2018).
289 These structures may also arise by internalization of large ERM-1::GFP^{+}structures from the
290 apical and basolateral PM of *vha-1* depleted worms (Fig 8B, S4 and Movie S3), which has
291 been linked to an autophagocytic process (Reinshagen et al., 2002). Since autophagosomes
292 and lysosomes have been linked to MVIs, we hypothesized that these structures undergo a
293 cytoplasmic elimination through these degradation pathways. Consistently, live tracking of
294 MVIs in *STXBP2* KO organoids revealed that MVIs are often surrounded by LAMP2^{+}
295 membranes and mostly disappear by cytoplasmic desintegration while the rest was eliminated
296 by PM fusion or cell shedding (Mosa et al., 2018). Interestingly, we found that irregular
297 MVIs induced by *vha-1(RNAi)* were often in close proximity to mixed organelles/lysosomes
298 (Fig 8C) and that some of the ERM-1^{+} MVIs were also positive for the lysosomal marker
299 LMP-1 (Fig 8D). Furthermore, some MVIs were also surrounded by a second membranous
300 layer positive for ERM-1 (Fig 8E). Considering that i) ezrin has been shown to accumulate at
301 the phagosome membrane and regulate phago-lysosomal fusion (Marion et al., 2011) and ii)

302 V0-ATPase extinction dramatically activates autophagy, as ascertained by the relocalization
303 of LGG-1::GFP (LC3 *C. elegans* ortholog) from the apical PM to cytoplasmic punctaes (Fig
304 8 G-H) (Chang et al., 2017), these data strongly suggest that MVIs are eliminated by
305 autophagosomes and/or lysosomes in *C. elegans* intestine, as proposed in mammals. This was
306 confirmed by timelapse microscopy on ERM-1^{+} MVIs, which progressively disintegrated in
307 the cytoplasm or inside ERM-1^{+} secondary structures (Fig 8F and Movie S4).
308

308

309 **Discussion**

310 By performing a double-RNAi screen in *C. elegans* intestine model we identified a
311 new function of the V0-ATPase complex as a critical determinant for the maintenance of one
312 of the most prominent cell surfaces, the absorptive apical PM of enterocytes. Our results
313 demonstrate that the V0-ATPase ensures the apical localization of polarity modules, brush
314 border components and trafficking factors, a major role that is substantiated by the severe
315 brush border defects consecutive to V0-ATPase depletion.

316 This study confirms the biological significance of systematic RNAi screens in *C.*
317 *elegans* to understand the complex mechanisms of polarity maintenance. Indeed, this model
318 has allowed to characterize the major role of membrane trafficking factors in epithelial
319 polarity maintenance including GSLs (Zhang et al., 2011), clathrin and its adaptor AP-1
320 (Shafaq-Zadah et al., 2012, Zhang et al., 2012), the kinase Lats/WTS-1 (Kang et al., 2009)
321 and the interactions between polarity proteins and membrane trafficking (Winter et al., 2012,
322 Balklava et al., 2007). Intriguingly, while interfering with Clathrin/AP-1, PAR-5 or GSLs
323 pathways induced a RAB-11^{+} endosomes loss and an inversion of both apical and basolateral
324 PM proteins polarity (Shafaq-Zadah et al., 2012, Zhang et al., 2012, Zhang et al., 2011,
325 Winter et al., 2012), we showed here that V0-ATPase silencing has a specific effect on brush
326 border and CDC-42/PAR polarity but not on transmembrane or basolateral proteins (Figs 2,
327 3). This surprising result points to a specific role of V0-ATPase in late trafficking events,
328 downstream of sorting factors such as GSLs, clathrin and AP-1, which is consistent with the
329 deleterious effect of GSLs biosynthesis enzyme or *aps-1* depletion on the localization of the
330 V0-ATPase subunit VHA-6 apical localization (Zhu et al., 2015). This conclusion is
331 supported by i) the known function of V0-ATPase in vesicle fusion to the plasma membrane
332 and its localisation in microvilli, ii) the accumulation of vesicles upon V0-ATPase depletion,

333 iii) the role of the SNARE SNAP-29 downstream of the V0-ATPase and iv) the phenotypic
334 similarities with the loss of Myosin 5B, STX3 or Munc18-2 in patients; indeed all these
335 factors have been found to control late trafficking events just upstream of, or during, the
336 fusion to the apical PM. In summary, clathrin/AP-1 (Shafaq-Zadah et al., 2012, Zhang et al.,
337 2012), GSLs (Zhang et al., 2011, Zhang et al., 2012) or the kinase Lats/WTS-1 (Kang et al.,
338 2009) might control sorting events, while V0-ATPase, Myosin 5B, STX3 or Munc18-2
339 would control late trafficking steps (Fig S5).

340 Furthermore, the genetic interaction experiments performed in this study advocate
341 that the two known sorting pathways, AP-1 and GSLs, converge towards RAB-11^{+}
342 endosomes and the V0-ATPase to ensure the polarized localization of soluble factors
343 necessary for intestinal polarity maintenance (i.e. the PAR module and ERM-1). First, AP-1
344 could regulate an early sorting step, which may rely on the recognition of sorting signals in
345 cargo proteins sequence, as shown previously for AP-1-dependent basolateral sorting through
346 di-leucin or tyrosine-based motifs (Bonifacino, 2014); the additional effect following the loss
347 of AP-1 and V0-ATPase suggests that the latter controls more than just AP-1-dependent
348 cargos. Second, GSLs could control a parallel early sorting step based on other signals (i.e.
349 GPI anchor) in a pathway encompassing also a V0-ATPase-dependent apical PM exocytosis,
350 based on the synthetic effect observed. Hence, we propose that polarity module and brush
351 border components undergo a complex apical PM targeting mechanism at both the TGN and
352 along the secretory/recycling pathways.

353 The precise mechanism by which the V0-ATPase controls the maintenance of the
354 intestinal polarity remains to be elucidated. The most studied function of this complex in
355 membrane trafficking relies on the H^{+}-pump-dependent (V0+V1 subunits) acidification of
356 intracellular organelles, which ensures their maturation and transport capacity (Maxson and
357 Grinstein, 2014). However, our results demonstrated a specific requirement for its V0-sector

358 in polarity maintenance, in an acidification-independent manner and likely through its already
359 characterized function in vesicle exocytosis (Hiesinger et al., 2005, Di Giovanni et al., 2010,
360 Baars et al., 2007, Liegeois et al., 2006). Indeed, the functional relevance of V0-ATPase
361 interaction with the fusion machinery has been demonstrated in many species, such as
362 drosophila or *T. marmorata*, where the V0-a1 subunit (V100 in drosophila) has been shown
363 to interact with the t-SNAREs Syx and SNAP25 (Hiesinger et al., 2005) and with the v-
364 SNARE VAMP-2 (Morel et al., 2003), respectively. Furthermore, the direct interaction
365 between the V0-c subunit (the ortholog of *vha-1*) and VAMP2 has been shown to be
366 indispensable for efficient synaptic vesicle fusion in mammalian cells (Di Giovanni et al.,
367 2010). A similar mechanism could take place for the apical exocytosis of vesicles containing
368 either polarity and brush border components, which may directly interact with the V0-
369 ATPase, and/or apical adaptor proteins, such as the ezrin partner NHERF-1/EBP50 that has
370 been recently found associated with the V-ATPase in interactome studies (Merkulova et al.,
371 2015). In line, we found that *vha-1(RNAi)* decreased the apical confinement of the SNARE
372 SNAP-29, a member of the SNAP23/25/29 family (Steegmaier et al., 1998) which seems to
373 be mislocalized in MVID mammalian models (Dhekne et al., 2018), and that *snap-29*
374 extinction phenocopies that of *vha-1* on *C. elegans* intestinal polarity. Considering that
375 SNAP-29 has been localized to RAB-11$^+$ endosomes in *C. elegans* (Kang et al., 2011), likely
376 at the terminal web (Fig 3) and that mammalian SNAP29 physically interacts with STX3
377 (Steegmaier et al., 1998), the V0-ATPase could directly interact with SNAP-29 to target the
378 exocytosis of RAB-11$^+$ endosomes and be involved in the same pathway than that of Myosin
379 5B/STX3/Munc18-2, which may also involve other trafficking factors, such as the N-
380 ethylmaleimide sensitive factor NSF-1/NSF (S1 Table).

381 Beyond disturbing polarity, we uncovered that V0-ATPase depletion induced severe
382 microvilli defects and the formation of MVIs that are typical features of MVID. MVID is a

383 devastating orphan congenital disorder of intestinal cells that manifested in intractable
384 diarrhoea and intestinal absorption defects appearing in early life of new-borns (Halac et al.,
385 2011, Ruemmele et al., 2006) and therapeutic avenues presently only rely on total parenteral
386 nutrition or small bowel transplantation (Halac et al., 2011). MVID originates from mutations
387 of MYO5B, STX3 or STXBP2 (Dhekne et al., 2018) that belong to the same apical
388 trafficking pathway. At the molecular level, a defective apical PM tethering of RAB-8^{+}/RAB-
389 11^{+} endosomes by the molecular motor Myosin 5B (Knowles et al., 2014) which interacts
390 with STX3 (Vogel et al., 2015) in concert with the sec/munc family protein Munc18-2 that
391 plays an accessory role for STX3-dependent vesicle tethering Munc18-2 (Vogel et al., 2017b)
392 has been proposed to be the major pathway leading to MVID phenotype. Hence, MVID is
393 strictly linked to a polarized trafficking defect and *in vitro* mammalian 2D or 3D cell culture
394 models have been developed to study its ill-defined underlying mechanisms, based on
395 Myosin 5B or Rab8/Rab11 depletion and disruption of Myosin 5B-Rab8/11 interaction (Feng
396 et al., 2017, Knowles et al., 2014, Engevik et al., 2018, Kravtsov et al., 2016, Weis et al.,
397 2016, Vogel et al., 2015, Schneeberger et al., 2015) as well as STX3 (Wiegerinck et al., 2014,
398 Vogel et al., 2015) or STXBP2 (Mosa et al., 2018, Vogel et al., 2017b) mutations.
399 However, some discrepancies were found while trying to integrate polarity
400 maintenance mechanisms identified *in vitro* and *in vivo*. For instance, while AP-1 was
401 renowned for basolateral sorting in cultured cells (Gravotta et al., 2012), its critical role in
402 apical traffic was characterized *in vivo* in *C. elegans* and in mouse (Shafaq-Zadah et al.,
403 2012, Zhang et al., 2012, Hase et al., 2013). While the *in vitro* culture of intestinal organoids
404 derived from MVID patients or MVID causing genes-deficient mouse (Schneeberger et al.,
405 2018, Mosa et al., 2018, Wiegerinck et al., 2014) and the mutation of *myosin5b*/*goosepimples*
406 in zebrafish (Sidhaye et al., 2016) seem to reproduce most of the cellular and structural
407 hallmarks of MVID, these models are not suitable for systematic studies. Conversely, the *in*

408 *vivo*, easy-to-use and screening amenable *C. elegans* model has been widely used to
409 understand intestinal polarity mechanisms (Zhu et al., 2015, Zhang et al., 2012, Winter et al.,
410 2012, Shafaq-Zadah et al., 2012, Kiela and Ghishan, 2016, Sobota et al., 2009, Kang et al.,
411 2009), but single deletion of the orthologs of MVID-causing genes (i.e. *hum-2*/*MYO5B*, *unc-*
412 *64*/*STX3*) seems not to induce an MVID phenotype (our unpublished observations), probably
413 due to compensatory mechanisms. We describe here for the first time a *C. elegans* model,
414 V0-ATPase depletion, that fully phenocopies the hallmarks of MVID (Table S3) and that
415 could be used to better characterize polarity maintenance mechanisms and MVID
416 pathophysiology. As a proof of principle, we studied the dynamics of MVIs, which onset and
417 elimination are still enigmatic. According to the "combined" model of MVI onset
418 (Schneeberger et al., 2018), in a recent paper using *STXBP2* KO organoids (Mosa et al.,
419 2018) and in the present study (Fig 7), we showed that MVIs may arise by two main
420 mechanisms; *de novo* nucleation in the cytoplasm or internalization of the PM. Both may rely
421 on the failure of apical exocytosis from RAB-11^{+} endosomes. Indeed, this defect would on
422 one hand result in the sequestration of polarity factors in the cytoplasm, that may be an
423 upstream signal to target newly-synthesized apical PAR, PM proteins and cytoskeleton and
424 consequently nucleate a new apical PM in the cytoplasm on accumulating vesicles. On the
425 other hand, defective exocytosis may lead to a local apical PM protein/lipid homeostasis
426 defect that would create a signal for endocytosis and targeting to autophagosomal-lysosomal
427 degradation, as proposed before (Reinshagen et al., 2002) and verified in this report (Fig 8).
428 Finally, we provide compelling evidence that V0-ATPase depletion fully phenocopies MVID
429 and this suggests that V0-ATPase may be involved in the aetiology of MVID and other
430 absorption disorders associated with apical PM defects, or affected in patients (Table S3).
431 Complementary use of both *C. elegans*, as a tool to screen for correctors of polarity
432 maintenance defects, as well as mammalian intestinal organoids or human samples to confirm

433 the conservation of V0-ATPase function, may lead to a better understanding of the
434 mechanisms of polarity maintenance as well as that of rare genetic enteropathies.
435

435

436 # Materials and methods

437

438 ***C. elegans* strains and maintenance**

439 Strains were maintained under typical conditions as described (Brenner, 1974). mNG and
440 mScarlet-tagged ERM-1, UNC-64 and PGP-1 were generated at the « Biologie de
441 *Cænorhabditis elegans* » facility (UMS3421, Lyon, France). The strains used in this study are
442 listed in Table S4.

443 **Gene silencing and screening by RNAi**

444 Larval RNAi was performed by feeding as described using the Ahringer-Source BioScience
445 library (Kamath and Ahringer, 2003, Shafaq-Zadah et al., 2012). Briefly, adult
446 hermaphrodites were bleached and transferred to RNAi plates containing HT115 *E. coli*
447 bacteria expressing the L4440 plasmid alone (control) or encoding the RNAi. For co-
448 depletion of *vha-1* and *aps-1*, equal amount of exponential phase bacterial culture (OD_{600}
449 ~0.6) were mixed together or with L4440 (single depletion). Developing worms were kept in
450 RNAi for 72-96h before mounting and imaging. RNAi specificity was verified by sequencing
451 and efficiency by target::GFP signal disappearance, as shown in Figures.

452 ***in vivo* confocal imaging using *C. elegans***

453 *C. elegans* imaging was performed *in vivo* by mounting the worms on a 10% agarose pad in a
454 solution of 100 nm polystyrene microbeads (Polysciences Inc.) to stop worm movement.
455 Confocal observations were performed using a Leica (Wetzlar, Germany) SPE equipped with
456 a 63X, 1.4 NA objective (LAS AF software) or a super-resolution Zeiss (Oberkochen,
457 Germany) LSM880 + Airyscan equipped with a 63X, 1.4 NA objective (Zen Black software).
458 All images were examined using Fiji software.

459 **TEM**

460 Control and RNAi worms (72-96 hours) were fixed by high-pressure freezing with
461 EMPACT-2 (Leica Microsystems) and then freeze substituted in anhydrous acetone
462 containing 1% OsO4, 0.5% glutaraldehyde and 0.25% uranyl acetate for 60 h in a freeze
463 substitution system (AFS-2; Leica Microsystems). Larvae were embedded in Epon-Araldite
464 mix (EMS hard formula). Adhesive frames were used (11560294 GENE-FRAME 65 µL,
465 Thermo Fisher Scientific) for flat-embedding, as previously described (Kolotuev et al., 2012),
466 to gain better antero-posterior orientation and sectioning. Ultrathin sections were cut on an
467 ultramicrotome (UC7; Leica Microsystems) and were collected on formvar-coated slot grids
468 (FCF2010-CU, EMS). Each larva was sectioned in 5 different places with ≥ 10 µm between
469 each grid to ensure that different cells were observed. Each grid contained at least 10
470 consecutive sections of 70 nm. TEM grids were observed using a JEM-1400 transmission
471 electron microscope (JEOL, Tokyo, Japan) operated at 120 kV, equipped with a Gatan Orius
472 SC 1000 camera (Gatan, Pleasanton, USA) and piloted by the Digital Micrograph program.
473 Micrographs were analyzed using Fiji software.

474 **Immuno-EM**

475 Immuno-electron microscopy was performed as described (Nicolle et al., 2015). For ultrathin
476 cryosections and immunogold labeling, larvae were fixed with 4% paraformaldehyde plus
477 0.1% glutaraldehyde in M9 buffer. Worms were embedded in 12% gelatin and infused in 2.3
478 M sucrose. Gelatin blocks were frozen and processed for ultracryomicrotomy (UC7cryo;
479 Leica Microsystems). Ultrathin cryosections (80 nm) were double-immunogold labeled and
480 analyzed by TEM as described above. We applied primary antibodies: rabbit anti-phospho-
481 ezrin (Thr567) / radixin (Thr564) / moes (Thr558) (1/100, 3149S Ozyme), detected using
482 protein A conjugated to 10 nm gold particles (PAG, 1/50, CMC, Utrecht, the Netherlands).

483 **Quantification**

484 Apical/cytoplasmic and basolateral/cytoplasmic ratios were calculated by quantifying the
485 signal intensity on a line covering the width of the apical PM and covering at least the length
486 of 2 adjacent intestinal cells. The intensity of the same line was quantified in the cytoplasm
487 underneath the PM. Basolateral ERM-1 appearance was calculated using the Plot Profile
488 function of Fiji, with a R.O.I. of 1.3 μm long crossing the highest basolateral PM intensity.
489 The 5 highest values were kept and divided by the mean fluorescence of the same R.O.I. in
490 the cytoplasm. Microvilli length and width were quantified using Fiji on 1) TEM pictures on
491 at least 5 sections per worm (Fig 4) or 2) on confocal pictures by calculating the width of at
492 least 4 lines of >100nm long/image (Fig 7). The number of RAB-5+ vesicles was quantified
493 using a home-made plugin for Fiji, as described (Gillard et al., 2015).

494 **Statistical analysis**

495 Results are presented as mean ± SEM of the number of independent experiments indicated in
496 the legends, and scattered dots represent individual worms. The total number of larvae used is
497 indicated in brackets in histograms. P values were calculated with the means of at least 3
498 independent experiments by two-tailed unpaired student's t-test and a 95% confidence level
499 was considered significant. Normal distribution of data and homogeneity of variance were
500 validated by calculating the skew factor (-2 > skew < 2) and the F-test, respectively. Mann-
501 Withney U-test and Krustal-Wallis test were used for calculating the P-values of non-normal
502 distributions and Welch correction was applied to normal distributions with non-homogenous
503 variances, as indicated in legends.

504

Acknowledgements

We thank Verena Gobel, Ken Kemphues, Jeremy Nance, Emily Troemel, Barth Grant and Ken Sato for strains. We also thank the « Biologie de *Cænorhabditis elegans* » facility (UMS3421, Lyon, France) which generated several CRISPR/Cas9 genome-edited strains used in this study. Some strains were provided by the CGC, which is funded by NIH Office of research Infrastructure Programs (P40 OD010440; University of Minnesota, USA). We thank Aurélien Perrin for the initial PAR-6::GFP screen, Raphaël Dima and Justine Cailloce for help with screen validation as well as Anne Pacquelet for critical reading of the manuscript and helpful discussions. Imaging was performed at the photonic and electron microscopy facilities of the Microscopy Rennes imaging Center (MRiC), Rennes, France. This work was supported by the Ligue Contre le Cancer Grand Ouest [22/29/35/72/41] and the Fondation Maladies Rares. ABM is the recipient of a postdoctoral fellowship from La Ligue Nationale Contre le Cancer (2017-2018).

Authors contribution

ABM, ON and MH performed and analyzed the experiments. ABM and GM designed the study and wrote the manuscript. GM supervised the study.

Conflict of interest

The authors declare no conflict of interest.

525 **References**

526 ALLMAN, E., JOHNSON, D. & NEHRKE, K. 2009. Loss of the apical V-ATPase a-subunit
527 VHA-6 prevents acidification of the intestinal lumen during a rhythmic behavior in C.
528 elegans. *Am J Physiol Cell Physiol,* 297**,** C1071-81.

529 BAARS, T. L., PETRI, S., PETERS, C. & MAYER, A. 2007. Role of the V-ATPase in
530 regulation of the vacuolar fission-fusion equilibrium. *Mol Biol Cell,* 18**,** 3873-82.

531 BALKLAVA, Z., PANT, S., FARES, H. & GRANT, B. D. 2007. Genome-wide analysis
532 identifies a general requirement for polarity proteins in endocytic traffic. *Nat Cell Biol,*
533 9**,** 1066-73.

534 BONIFACINO, J. S. 2014. Adaptor proteins involved in polarized sorting. *J Cell Biol,* 204**,** 7-
535 17.

536 BRENNER, S. 1974. The genetics of Caenorhabditis elegans. *Genetics,* 77**,** 71-94.

537 BRYANT, D. M., DATTA, A., RODRIGUEZ-FRATICELLI, A. E., PERANEN, J., MARTIN-
538 BELMONTE, F. & MOSTOV, K. E. 2010. A molecular network for de novo generation
539 of the apical surface and lumen. *Nat Cell Biol,* 12**,** 1035-45.

540 CHANG, J. T., KUMSTA, C., HELLMAN, A. B., ADAMS, L. M. & HANSEN, M. 2017.
541 Spatiotemporal regulation of autophagy during Caenorhabditis elegans aging. *Elife,*
542 6.

543 COLLACO, A. M., GEIBEL, P., LEE, B. S., GEIBEL, J. P. & AMEEN, N. A. 2013. Functional
544 vacuolar ATPase (V-ATPase) proton pumps traffic to the enterocyte brush border
545 membrane and require CFTR. *Am J Physiol Cell Physiol,* 305**,** C981-96.

546 COLOMBIE, N., CHOESMEL-CADAMURO, V., SERIES, J., EMERY, G., WANG, X. &
547 RAMEL, D. 2017. Non-autonomous role of Cdc42 in cell-cell communication during
548 collective migration. *Dev Biol,* 423**,** 12-18.

549 CRAWLEY, S. W., MOOSEKER, M. S. & TYSKA, M. J. 2014. Shaping the intestinal brush
550 border. *J Cell Biol,* 207**,** 441-51.

551 DESCLOZEAUX, M., VENTURATO, J., WYLIE, F. G., KAY, J. G., JOSEPH, S. R., LE, H. T.
552 & STOW, J. L. 2008. Active Rab11 and functional recycling endosome are required
553 for E-cadherin trafficking and lumen formation during epithelial morphogenesis. *Am J*
554 *Physiol Cell Physiol,* 295**,** C545-56.

555 DHEKNE, H. S., HSIAO, N. H., ROELOFS, P., KUMARI, M., SLIM, C. L., RINGS, E. H. &
556 VAN IJZENDOORN, S. C. 2014. Myosin Vb and Rab11a regulate phosphorylation of
557 ezrin in enterocytes. *J Cell Sci,* 127**,** 1007-17.

558 DHEKNE, H. S., PYLYPENKO, O., OVEREEM, A. W., FERREIRA, R. J., VAN DER VELDE,
559 K. J., RINGS, E., POSOVSZKY, C., SWERTZ, M. A., HOUDUSSE, A. & VAN, I. S.
560 C. D. 2018. MYO5B, STX3, and STXBP2 mutations reveal a common disease
561 mechanism that unifies a subset of congenital diarrheal disorders: A mutation update.
562 *Hum Mutat,* 39**,** 333-344.

563 DI GIOVANNI, J., BOUDKKAZI, S., MOCHIDA, S., BIALOWAS, A., SAMARI, N., LEVEQUE,
564 C., YOUSSOUF, F., BRECHET, A., IBORRA, C., MAULET, Y., MOUTOT, N.,
565 DEBANNE, D., SEAGAR, M. & EL FAR, O. 2010. V-ATPase membrane sector
566 associates with synaptobrevin to modulate neurotransmitter release. *Neuron,* 67**,**
567 268-79.

568 ENGEVIK, A. C., KAJI, I., ENGEVIK, M. A., MEYER, A. R., WEIS, V. G., GOLDSTEIN, A.,
569 HESS, M. W., MULLER, T., KOEPSELL, H., DUDEJA, P. K., TYSKA, M., HUBER, L.
570 A., SHUB, M. D., AMEEN, N. & GOLDENRING, J. R. 2018. Loss of MYO5B Leads to
571 Reductions in Na(+) Absorption With Maintenance of CFTR-Dependent Cl(-)
572 Secretion in Enterocytes. *Gastroenterology*.

573 FENG, Q., BONDER, E. M., ENGEVIK, A. C., ZHANG, L., TYSKA, M. J., GOLDENRING, J.
574 R. & GAO, N. 2017. Disruption of Rab8a and Rab11a causes formation of
575 basolateral microvilli in neonatal enteropathy. *J Cell Sci,* 130**,** 2491-2505.

576 FORGAC, M. 2007. Vacuolar ATPases: rotary proton pumps in physiology and
577 pathophysiology. *Nat Rev Mol Cell Biol,* 8**,** 917-29.

578 GILLARD, G., SHAFAQ-ZADAH, M., NICOLLE, O., DAMAJ, R., PECREAUX, J. &
579 MICHAUX, G. 2015. Control of E-cadherin apical localisation and morphogenesis by
580 a SOAP-1/AP-1/clathrin pathway in C. elegans epidermal cells. *Development,* 142**,**
581 1684-94.

582 GRAVOTTA, D., CARVAJAL-GONZALEZ, J. M., MATTERA, R., DEBORDE, S.,
583 BANFELDER, J. R., BONIFACINO, J. S. & RODRIGUEZ-BOULAN, E. 2012. The
584 Clathrin Adaptor AP-1A Mediates Basolateral Polarity. *Dev Cell,* 22**,** 811-23.

585 GUO, B., LIANG, Q., LI, L., HU, Z., WU, F., ZHANG, P., MA, Y., ZHAO, B., KOVACS, A. L.,
586 ZHANG, Z., FENG, D., CHEN, S. & ZHANG, H. 2014. O-GlcNAc-modification of
587 SNAP-29 regulates autophagosome maturation. *Nat Cell Biol,* 16**,** 1215-26.

588 HALAC, U., LACAILLE, F., JOLY, F., HUGOT, J. P., TALBOTEC, C., COLOMB, V.,
589 RUEMMELE, F. M. & GOULET, O. 2011. Microvillous inclusion disease: how to
590 improve the prognosis of a severe congenital enterocyte disorder. *J Pediatr*
591 *Gastroenterol Nutr,* 52**,** 460-5.

592 HASE, K., NAKATSU, F., OHMAE, M., SUGIHARA, K., SHIODA, N., TAKAHASHI, D.,
593 OBATA, Y., FURUSAWA, Y., FUJIMURA, Y., YAMASHITA, T., FUKUDA, S.,
594 OKAMOTO, H., ASANO, M., YONEMURA, S. & OHNO, H. 2013. AP-1B-Mediated
595 Protein Sorting Regulates Polarity and Proliferation of Intestinal Epithelial Cells in
596 Mice. *Gastroenterology,* 145**,** 625-35.

597 HEGAN, P. S., GIRAL, H., LEVI, M. & MOOSEKER, M. S. 2012. Myosin VI is required for
598 maintenance of brush border structure, composition, and membrane trafficking
599 functions in the intestinal epithelial cell. *Cytoskeleton (Hoboken),* 69**,** 235-51.

600 HEIN, Z., SCHMIDT, S., ZIMMER, K. P. & NAIM, H. Y. 2011. The dual role of annexin II in
601 targeting of brush border proteins and in intestinal cell polarity. *Differentiation,* 81**,**
602 243-52.

603 HEINTZELMAN, M. B. & MOOSEKER, M. S. 1990a. Assembly of the brush border
604 cytoskeleton: changes in the distribution of microvillar core proteins during enterocyte
605 differentiation in adult chicken intestine. *Cell Motil Cytoskeleton,* 15**,** 12-22.

606 HEINTZELMAN, M. B. & MOOSEKER, M. S. 1990b. Structural and compositional analysis
607 of early stages in microvillus assembly in the enterocyte of the chick embryo.
608 *Differentiation,* 43**,** 175-82.

609 HIESINGER, P. R., FAYYAZUDDIN, A., MEHTA, S. Q., ROSENMUND, T., SCHULZE, K. L.,
610 ZHAI, R. G., VERSTREKEN, P., CAO, Y., ZHOU, Y., KUNZ, J. & BELLEN, H. J.
611 2005. The v-ATPase V0 subunit a1 is required for a late step in synaptic vesicle
612 exocytosis in Drosophila. *Cell,* 121**,** 607-20.

613 IANCU, T. C., MAHAJNAH, M., MANOV, I. & SHAOUL, R. 2007. Microvillous inclusion
614 disease: ultrastructural variability. *Ultrastruct Pathol,* 31**,** 173-88.

615 JI, Y. J., CHOI, K. Y., SONG, H. O., PARK, B. J., YU, J. R., KAGAWA, H., SONG, W. K. &
616 AHNN, J. 2006. VHA-8, the E subunit of V-ATPase, is essential for pH homeostasis
617 and larval development in C. elegans. *FEBS Lett,* 580**,** 3161-6.

618 KAMATH, R. S. & AHRINGER, J. 2003. Genome-wide RNAi screening in Caenorhabditis
619 elegans. *Methods,* 30**,** 313-21.

620 KANG, J., BAI, Z., ZEGAREK, M. H., GRANT, B. D. & LEE, J. 2011. Essential roles of snap-
621 29 in C. elegans. *Dev Biol,* 355**,** 77-88.

622 KANG, J., SHIN, D., YU, J. R. & LEE, J. 2009. Lats kinase is involved in the intestinal apical
623 membrane integrity in the nematode Caenorhabditis elegans. *Development,* 136**,**
624 2705-15.

625 KIELA, P. R. & GHISHAN, F. K. 2016. Physiology of Intestinal Absorption and Secretion.
626 *Best Pract Res Clin Gastroenterol,* 30**,** 145-59.

627 KNIGHT, A. J., JOHNSON, N. M. & BEHM, C. A. 2012. VHA-19 is essential in
628 Caenorhabditis elegans oocytes for embryogenesis and is involved in trafficking in
629 oocytes. *PLoS One,* 7**,** e40317.

630 KNOWLES, B. C., ROLAND, J. T., KRISHNAN, M., TYSKA, M. J., LAPIERRE, L. A.,
631 DICKMAN, P. S., GOLDENRING, J. R. & SHUB, M. D. 2014. Myosin Vb uncoupling
632 from RAB8A and RAB11A elicits microvillus inclusion disease. *J Clin Invest,* 124**,**
633 2947-62.

634 KOLOTUEV, I., BUMBARGER, D. J., LABOUESSE, M. & SCHWAB, Y. 2012. Targeted
635 ultramicrotomy: a valuable tool for correlated light and electron microscopy of small
636 model organisms. *Methods Cell Biol,* 111**,** 203-22.

637 KRAVTSOV, D. V., AHSAN, M. K., KUMARI, V., VAN IJZENDOORN, S. C., REYES-
638 MUGICA, M., KUMAR, A., GUJRAL, T., DUDEJA, P. K. & AMEEN, N. A. 2016.
639 Identification of intestinal ion transport defects in microvillus inclusion disease. *Am J*
640 *Physiol Gastrointest Liver Physiol,* 311**,** G142-55.

641 LEE, S. K., LI, W., RYU, S. E., RHIM, T. & AHNN, J. 2010. Vacuolar (H+)-ATPases in
642 Caenorhabditis elegans: what can we learn about giant H+ pumps from tiny worms?
643 *Biochim Biophys Acta,* 1797**,** 1687-95.

644 LIEGEOIS, S., BENEDETTO, A., GARNIER, J. M., SCHWAB, Y. & LABOUESSE, M. 2006.
645 The V0-ATPase mediates apical secretion of exosomes containing Hedgehog-related
646 proteins in Caenorhabditis elegans. *J Cell Biol,* 173**,** 949-61.

647 MARION, S., HOFFMANN, E., HOLZER, D., LE CLAINCHE, C., MARTIN, M., SACHSE, M.,
648 GANEVA, I., MANGEAT, P. & GRIFFITHS, G. 2011. Ezrin promotes actin assembly
649 at the phagosome membrane and regulates phago-lysosomal fusion. *Traffic,* 12**,** 421-
650 37.

651 MARTIN-BELMONTE, F., GASSAMA, A., DATTA, A., YU, W., RESCHER, U., GERKE, V. &
652 MOSTOV, K. 2007. PTEN-mediated apical segregation of phosphoinositides controls
653 epithelial morphogenesis through Cdc42. *Cell,* 128**,** 383-97.

654 MAXSON, M. E. & GRINSTEIN, S. 2014. The vacuolar-type H(+)-ATPase at a glance - more
655 than a proton pump. *J Cell Sci,* 127**,** 4987-93.

656 MCGHEE, J. D. 2007. The C. elegans intestine. *WormBook***,** 1-36.

657 MERKULOVA, M., PAUNESCU, T. G., AZROYAN, A., MARSHANSKY, V., BRETON, S. &
658 BROWN, D. 2015. Mapping the H(+) (V)-ATPase interactome: identification of
659 proteins involved in trafficking, folding, assembly and phosphorylation. *Sci Rep,* 5**,**
660 14827.

661 MICHAUX, G., MASSEY-HARROCHE, D., NICOLLE, O., RABANT, M., BROUSSE, N.,
662 GOULET, O., LE BIVIC, A. & RUEMMELE, F. M. 2016. The localisation of the apical
663 Par/Cdc42 polarity module is specifically affected in microvillus inclusion disease.
664 *Biol Cell,* 108**,** 19-28.

665 MOREL, N., DEDIEU, J. C. & PHILIPPE, J. M. 2003. Specific sorting of the a1 isoform of the
666 V-H+ATPase a subunit to nerve terminals where it associates with both synaptic
667 vesicles and the presynaptic plasma membrane. *J Cell Sci,* 116**,** 4751-62.

668 MOSA, M. H., NICOLLE, O., MASCHALIDI, S., SEPULVEDA, F. E., BIDAUD-MEYNARD,
669 A., MENCHE, C., MICHELS, B. E., MICHAUX, G., DE SAINT BASILE, G. & FARIN,
670 H. F. 2018. Dynamic Formation of Microvillus Inclusions During Enterocyte
671 Differentiation in Munc18-2-Deficient Intestinal Organoids. *Cell Mol Gastroenterol*
672 *Hepatol,* 6**,** 477-493 e1.

673 MULLER, T., HESS, M. W., SCHIEFERMEIER, N., PFALLER, K., EBNER, H. L., HEINZ-
674 ERIAN, P., PONSTINGL, H., PARTSCH, J., ROLLINGHOFF, B., KOHLER, H.,
675 BERGER, T., LENHARTZ, H., SCHLENCK, B., HOUWEN, R. J., TAYLOR, C. J.,
676 ZOLLER, H., LECHNER, S., GOULET, O., UTERMANN, G., RUEMMELE, F. M.,
677 HUBER, L. A. & JANECKE, A. R. 2008. MYO5B mutations cause microvillus
678 inclusion disease and disrupt epithelial cell polarity. *Nat Genet,* 40**,** 1163-5.

679 NICOLLE, O., BUREL, A., GRIFFITHS, G., MICHAUX, G. & KOLOTUEV, I. 2015.
680 Adaptation of Cryo-Sectioning for IEM Labeling of Asymmetric Samples: A Study
681 Using Caenorhabditis elegans. *Traffic,* 16**,** 893-905.

682 REINSHAGEN, K., NAIM, H. Y. & ZIMMER, K. P. 2002. Autophagocytosis of the apical
683 membrane in microvillus inclusion disease. *Gut,* 51**,** 514-21.

684 RODRIGUEZ-BOULAN, E. & MACARA, I. G. 2014. Organization and execution of the
685 epithelial polarity programme. *Nat Rev Mol Cell Biol,* 15**,** 225-42.

686 RUEMMELE, F. M., SCHMITZ, J. & GOULET, O. 2006. Microvillous inclusion disease
687 (microvillous atrophy). *Orphanet J Rare Dis,* 1**,** 22.

688 SAEGUSA, K., SATO, M., SATO, K., NAKAJIMA-SHIMADA, J., HARADA, A. & SATO, K.
689 2014. Caenorhabditis elegans chaperonin CCT/TRiC is required for actin and tubulin
690 biogenesis and microvillus formation in intestinal epithelial cells. *Mol Biol Cell,* 25**,**
691 3095-104.

692 SATO, M., SAEGUSA, K., SATO, K., HARA, T., HARADA, A. & SATO, K. 2011.
693 Caenorhabditis elegans SNAP-29 is required for organellar integrity of the
694 endomembrane system and general exocytosis in intestinal epithelial cells. *Mol Biol*
695 *Cell,* 22**,** 2579-87.

696 SCHNEEBERGER, K., ROTH, S., NIEUWENHUIS, E. E. S. & MIDDENDORP, S. 2018.
697 Intestinal epithelial cell polarity defects in disease: lessons from microvillus inclusion
698 disease. *Dis Model Mech,* 11.

699 SCHNEEBERGER, K., VOGEL, G. F., TEUNISSEN, H., VAN OMMEN, D. D., BEGTHEL,
700 H., EL BOUAZZAOUI, L., VAN VUGT, A. H., BEEKMAN, J. M., KLUMPERMAN, J.,
701 MULLER, T., JANECKE, A., GERNER, P., HUBER, L. A., HESS, M. W., CLEVERS,
702 H., VAN ES, J. H., NIEUWENHUIS, E. E. & MIDDENDORP, S. 2015. An inducible

703 mouse model for microvillus inclusion disease reveals a role for myosin Vb in apical
704 and basolateral trafficking. *Proc Natl Acad Sci U S A,* 112**,** 12408-13.

705 SHAFAQ-ZADAH, M., BROCARD, L., SOLARI, F. & MICHAUX, G. 2012. AP-1 is required
706 for the maintenance of apico-basal polarity in the C. elegans intestine. *Development,*
707 139**,** 2061-70.

708 SIDHAYE, J., PINTO, C. S., DHARAP, S., JACOB, T., BHARGAVA, S. & SONAWANE, M.
709 2016. The zebrafish goosepimples/myosin Vb mutant exhibits cellular attributes of
710 human microvillus inclusion disease. *Mech Dev,* 142**,** 62-74.

711 SOBAJIMA, T., YOSHIMURA, S., IWANO, T., KUNII, M., WATANABE, M., ATIK, N.,
712 MUSHIAKE, S., MORII, E., KOYAMA, Y., MIYOSHI, E. & HARADA, A. 2014. Rab11a
713 is required for apical protein localisation in the intestine. *Biol Open,* 4**,** 86-94.

714 SOBOTA, J. A., BACK, N., EIPPER, B. A. & MAINS, R. E. 2009. Inhibitors of the V0 subunit
715 of the vacuolar H+-ATPase prevent segregation of lysosomal- and secretory-pathway
716 proteins. *J Cell Sci,* 122**,** 3542-53.

717 STEEGMAIER, M., YANG, B., YOO, J. S., HUANG, B., SHEN, M., YU, S., LUO, Y. &
718 SCHELLER, R. H. 1998. Three novel proteins of the syntaxin/SNAP-25 family. *J Biol*
719 *Chem,* 273**,** 34171-9.

720 SUDHOF, T. C. & ROTHMAN, J. E. 2009. Membrane fusion: grappling with SNARE and SM
721 proteins. *Science,* 323**,** 474-7.

722 TALMON, G., HOLZAPFEL, M., DIMAIO, D. J. & MUIRHEAD, D. 2012. Rab11 is a useful
723 tool for the diagnosis of microvillous inclusion disease. *Int J Surg Pathol,* 20**,** 252-6.

724 VACCA, B., BAZELLIERES, E., NOUAR, R., HARADA, A., MASSEY-HARROCHE, D. & LE
725 BIVIC, A. 2014. Drebrin E depletion in human intestinal epithelial cells mimics Rab8a
726 loss of function. *Hum Mol Genet,* 23**,** 2834-46.

727 VOGEL, G. F., HESS, M. W., PFALLER, K., HUBER, L. A., JANECKE, A. R. & MULLER, T.
728 2016. Towards understanding microvillus inclusion disease. *Mol Cell Pediatr,* 3**,** 3.

729 VOGEL, G. F., JANECKE, A. R., KRAINER, I. M., GUTLEBEN, K., WITTING, B., MITTON,
730 S. G., MANSOUR, S., BALLAUFF, A., ROLAND, J. T., ENGEVIK, A. C., CUTZ, E.,
731 MULLER, T., GOLDENRING, J. R., HUBER, L. A. & HESS, M. W. 2017a. Abnormal
732 Rab11-Rab8-vesicles cluster in enterocytes of patients with microvillus inclusion
733 disease. *Traffic,* 18**,** 453-464.

734 VOGEL, G. F., KLEE, K. M., JANECKE, A. R., MULLER, T., HESS, M. W. & HUBER, L. A.
735 2015. Cargo-selective apical exocytosis in epithelial cells is conducted by Myo5B,
736 Slp4a, Vamp7, and Syntaxin 3. *J Cell Biol,* 211**,** 587-604.

737 VOGEL, G. F., VAN RIJN, J. M., KRAINER, I. M., JANECKE, A. R., POSOVSZKY, C.,
738 COHEN, M., SEARLE, C., JANTCHOU, P., ESCHER, J. C., PATEY, N., CUTZ, E.,
739 MULLER, T., MIDDENDORP, S., HESS, M. W. & HUBER, L. A. 2017b. Disrupted
740 apical exocytosis of cargo vesicles causes enteropathy in FHL5 patients with
741 Munc18-2 mutations. *JCI Insight,* 2.

742 WEIS, V. G., KNOWLES, B. C., CHOI, E., GOLDSTEIN, A. E., WILLIAMS, J. A., MANNING,
743 E. H., ROLAND, J. T., LAPIERRE, L. A. & GOLDENRING, J. R. 2016. Loss of
744 MYO5B in mice recapitulates Microvillus Inclusion Disease and reveals an apical
745 trafficking pathway distinct to neonatal duodenum. *Cell Mol Gastroenterol Hepatol,* 2**,**
746 131-157.

747 WIEGERINCK, C. L., JANECKE, A. R., SCHNEEBERGER, K., VOGEL, G. F., VAN
748 HAAFTEN-VISSER, D. Y., ESCHER, J. C., ADAM, R., THONI, C. E., PFALLER, K.,
749 JORDAN, A. J., WEIS, C. A., NIJMAN, I. J., MONROE, G. R., VAN HASSELT, P. M.,
750 CUTZ, E., KLUMPERMAN, J., CLEVERS, H., NIEUWENHUIS, E. E., HOUWEN, R.
751 H., VAN HAAFTEN, G., HESS, M. W., HUBER, L. A., STAPELBROEK, J. M.,
752 MULLER, T. & MIDDENDORP, S. 2014. Loss of syntaxin 3 causes variant
753 microvillus inclusion disease. *Gastroenterology,* 147**,** 65-68 e10.

754 WINTER, J. F., HOPFNER, S., KORN, K., FARNUNG, B. O., BRADSHAW, C. R.,
755 MARSICO, G., VOLKMER, M., HABERMANN, B. & ZERIAL, M. 2012.
756 Caenorhabditis elegans screen reveals role of PAR-5 in RAB-11-recycling endosome
757 positioning and apicobasal cell polarity. *Nat Cell Biol,* 14**,** 666-76.

758 ZHANG, H., ABRAHAM, N., KHAN, L. A., HALL, D. H., FLEMING, J. T. & GOBEL, V. 2011.
759 Apicobasal domain identities of expanding tubular membranes depend on
760 glycosphingolipid biosynthesis. *Nat Cell Biol,* 13**,** 1189-201.

761 ZHANG, H., KIM, A., ABRAHAM, N., KHAN, L. A., HALL, D. H., FLEMING, J. T. & GOBEL,
762 V. 2012. Clathrin and AP-1 regulate apical polarity and lumen formation during C.
763 elegans tubulogenesis. *Development,* 139**,** 2071-83.

764 ZHU, H., SEWELL, A. K. & HAN, M. 2015. Intestinal apical polarity mediates regulation of
765 TORC1 by glucosylceramide in C. elegans. *Genes Dev,* 29**,** 1218-23.
766

767

767 **Figure 1. V0-ATPase controls the apical localization of polarity and brush border**
768 **components.** (A-C) Larvae expressing endogenous ERM-1::mNG, PAR-6::GFP and
769 GFP::PKC-3 were imaged after 72h silencing of V0-ATPase (*vha-1(RNAi))* or V1-ATPase
770 (*vha-8(RNAi))* subunits. Arrows show the intestinal apical PM. Arrowheads show the
771 basolateral mislocalization of markers upon *vha-1(RNAi)*. The percentage of worms
772 displaying basolateral PAR polarity markers and the number of worms analyzed are indicated
773 on each panel. (D-F) Quantification of the apical/cytoplasmic (Ap/cyto) ratio of ERM-
774 1::mNG (D), PAR-6::GFP (E) and GFP::PKC-3 (F) upon 72h silencing of V0-ATPase (*vha-*
775 *1*, *-4*, *-19*) or V1-ATPase (*vha-8, -15*) subunits (n=3-5 independent experiments). (G) V0-
776 ATPase subunits (*vha-1, -4, -19*) knockdown specifically induces a basolateral relocalization
777 of ERM-1. Histogram shows the basolateral/cytoplasmic (Bl/cyto) ratio of ERM-1::mNG.
778 Dotted red line indicates a ratio of 1, which means no basolateral localization. (H-K) V0-
779 ATPase silencing does not affect the polarity of the apical transmembrane proteins PEPT-1
780 and PGP-1. Strains expressing exogenously (PEPT-1) or endogenously (PGP-1)-tagged
781 markers were silenced for *vha-1* or *vha-8* during 72h and imaged. Histograms in (J-K)
782 represent the quantification of the Ap/cyto ratio. Arrows show the intestinal apical PM.
783 Arrowheads show the basolateral mislocalization of markers upon *vha-1(RNAi)*. Histograms
784 are mean ± SEM, dots represent individual worms and total number of worms from 3
785 independent experiments is indicated in brackets. n.s., non-significant, *p<0.05, **p<0.01,
786 ***p<0.001, ****p<0.0001. Scale bars, 5 μm.
787

787

788 **Figure 2. V0-ATPase affects apical trafficking via RAB-11 apical recycling endosomes**.
789 (A-C) V-ATPase complex silencing affects the morphology of lysosomes. (A) Ultrastructural
790 characterization of transversely-sectioned control (L4440), V0-ATPase (*vha-1*) or V1-
791 ATPase (*vha-8*) depleted worms (72h RNAi). While lysosomes with normal morphology and
792 size (~0.5μm) were rarely observed in control worms (left panel, arrowhead and insert),
793 cytoplasmic enlarged "mixed organelles" with distinct lysosomal and vesicular regions were
794 observed upon both *vha-1* and *vha-8(RNAi)* (arrows). (B) Quantification of the number of
795 mixed organelles (n=1-5grid/larvae, n=7-13 larvae). (C) shows the accumulation of the
796 lysosomal marker LMP-1::GFP in large cytoplasmic structures (arrowheads) upon both *vha-1*
797 and *vha-8(RNAi)*. (D) Ultrastructural characterization of transversely-sectioned control
798 (L4440), V0-ATPase (*vha-1*) and V1-ATPase (*vha-8*) depleted worms. Middle panel shows a
799 specific and massive accumulation of cytoplasmic electron-lucent vesicles upon *vha-1(RNAi)*.
800 (E-H) V0- or V1-ATPase silencing marginally decreases the number of RAB-5^{+} vesicles but
801 V0-ATPase knockdown specifically disrupts RAB-11^{+} apical recycling endosomes. Confocal
802 imaging of the endosomal markers of apical early/sorting (RAB-5, E) and apical recycling
803 (RAB-11, G) endosomes in control, *vha-1(RNAi)* and *vha-8(RNAi)* conditions. (F-H)
804 Quantification of the number of RAB-5+ vesicles (F) and RAB-11 apical/cytoplasmic
805 (Ap/cyto) ratio (H) (n=3). (I-J) *rab-11(RNAi)* phenocopies V0-ATPase depletion on ERM-
806 1::GFP polarity. ERM-1::GFP expressing worms were silenced for *rab-11* during 72h and
807 imaged. Arrowheads show the basolateral accumulation of ERM-1. (J) shows ERM-1
808 basolateral/cytoplasmic (Bl/cyto) ratio quantification (n=3). Histograms are mean ± SEM on
809 each panel, dots represent individual worms and the total number of worms from 3
810 independent experiments is indicated in brackets. L, lumen; mv, microvilli; Ly, lysosome.

811 n.s., non-significant, *p<0.05, ***p<0.001, ****p<0.0001. Scale bars, 0.2 or 0.5μm (A, D)

812 and 5 μm (C, E, G, I).

813

813

814 **Figure 3. SNAP-29 acts downstream of V0-ATPase in polarity maintenance.**

815 (A-C) V0-ATPase silencing specifically decreases the apical localization of SNAP-29::GFP.
816 Strains expressing the indicated markers were silenced for V0- (*vha-1*) or V1-(*vha-8*) ATPase
817 during 72h and imaged. Histograms represent the quantification of the apical/cytoplasmic
818 (Ap/cyto) ratio of each marker. (D-E) *snap-29(RNAi)* induces a basolateral localization of
819 ERM-1. *snap-29* was knocked down by RNAi in ERM-1::GFP-expressing strains and its
820 localization was recorded after 72h. (E) represents the quantification of the
821 basolateral/cytoplasmic (Bl/cyto) ratio of ERM-1::GFP. (F-G) *snap-29(RNAi)* also induces a
822 RAB-11 endosomes loss but does not affect VHA-6 apical localization. *snap-29* was depleted
823 by RNAi in a strain co-expressing RAB-11::GFP and VHA-6::mCh. Arrows and arrowheads
824 indicate the apical and basolateral PM, respectively. The asterisk shows muscular Myo-
825 3P::GFP co-expressed with VHA-6::mCh. (G) shows the quantification of RAB-11::GFP
826 (left panel) and VHA-6::mCh (right panel) apical/cytoplasmic ratio (Ap/cyto). Histograms
827 are mean ± SEM on each panel, dots represent individual worms and the total number of
828 worms from 3 (A-C, E) and 2 (G) independent experiments is indicated in brackets. n.s., non-
829 significant, *$p<0.05$, **$p<0.01$, ****$p<0.0001$. Scale bars, 5 μm.

830

830

831 **Figure 4. Super-resolution imaging of the intestinal apical PM.**

832 (A-D) Strains expressing the indicated markers were mounted and imaged. * indicates
833 endogenously-tagged markers, arrowheads and arrows indicate microvilli and presumptive
834 terminal web, respectively. Scale bars, 2 μm.

835

835

836 **Figure 5. V0-ATPase genetically interacts with GSLs in intestinal polarity maintenance.**
837 (A) *vha-1* and *aps-1(RNAi)* additionally induce a basolateral mislocalization of ERM-1. *C.*
838 *elegans* worms expressing ERM-1::GFP were silenced for control (L4440) or a mix of
839 control, *vha-1* or *aps-1(RNAi)* as indicated and the basolateral/cytoplasmic ratio of ERM-
840 1::GFP (Bl/cyto) was quantified. (B-C) V0-ATPase and GSLs synergistically control
841 intestinal polarity maintenance. ERM-1::GFP expressing wild type and *let-767, sDp3* loss-of-
842 function strains were silenced for *vha-1*. (B) shows the quantification of ERM-1::GFP
843 Bl/cyto ratio and (C) a representative experiment. Histograms are mean ± SEM on each
844 panel, dots represent individual worms and the total number of worms from 3 independent
845 experiments is indicated in brackets. Arrows and arrowheads show the apical and basolateral
846 PM, respectively. Scale bar, 5µm. Krustal-Wallis test. n.s. non-significant, *$p<0.05$,
847 **$p<0.01$, ***$p<0.001$, ****$p<0.0001$.
848

848

849 **Figure 6. V0-ATPase depletion induces microvillus atrophy in *C. elegans***

850 (A) Visualization of microvilli by super-resolution (upper panels, 96h RNAi, ERM-1::GFP)
851 and TEM (lower panels, 72h RNAi) analysis. Control animals showed the typical intestinal
852 brush border morphology consisting of a dense brush border of microvilli surrounded by a
853 glycocalyx and stabilized by the terminal web, a network of actin and intermediate filaments
854 running below and in parallel to the apical plasma membrane. Conversely, *vha-1(RNAi)*
855 worms display a microvillus atrophy, with irregular, shorter and sparse microvilli, a
856 phenotype that is not observed in *vha-8* depleted worms. The terminal web appears normal in
857 all cases. L, lumen; mv, microvilli; tw, terminal web. (B-C) Measurement of microvilli length
858 (B) and width (C) upon 72h V0 and V1-ATPase knockdown from TEM images. Data are
859 mean ± SEM, n=5 microvilli/worm on the number of worms indicated in brackets. n.s., non-
860 significant, ***p<0,001, ****p<0.0001. (D-E) The brush border components ACT-5 and
861 ERM-1 localize to the basolateral PM with a microvilli-like pattern upon 96h *vha-1(RNAi)*.
862 Lower panels are magnified images of the selected areas. Scale bar size is shown on each
863 panel.

864

864

865 **Figure 7. V0-ATPase silencing induces MVID in *C. elegans***

866 (A-B) 96h V0-ATPase knockdown (*vha-1(RNAi)*) induces the formation of cytoplasmic
867 ERM-1$^+$ and ACT-5$^+$ microvillus inclusion-like structures. (C) Line scan shows that rounded
868 structures found in the cytoplasm (lower panel) display periodic pattern reminiscent of apical
869 microvilli (upper panel). A line scan of 4 μm was performed (dotted line) on ERM-1::mNG
870 expressing worms apical PM (control worms) and on ERM-1::mNG$^+$ MVI-like structures
871 (96h of *vha-1(RNAi)*). (D-E) GFP::PKC-3 and SNAP-29::GFP localize to *vha-1(RNAi)*
872 induced MVI-like structures. Insert is a magnified image of the structure indicated by the
873 arrowhead. (F-H) V0-ATPase silencing mostly induces cytoplasmic ERM-1$^+$
874 vacuoles/irregular MVIs as well as typical MVIs. (F-G) Ultrastructural analysis of
875 cytoplasmic inclusions observed in *C. elegans* silenced for *vha-1* during 96h by TEM. Note
876 the classical MVIs showing the symmetrical, mainly inward-pointing arrangement of
877 microvilli (arrowheads) and the area around the inclusion corresponding to the terminal web
878 (arrows). Typical MVIs were found in 3/16 worms. (G) Numerous and larger 'irregular'
879 vacuole-inclusions with a wide heterogeneity in size, shape, and electron-density were found
880 upon 96h *vha-1* silencing. The lumen contains probably amorphous, microvesicular,
881 membranous and lipid components. (H) Immuno-EM analysis of vacuole-like structures
882 using phospho-ezrin antibody and nanogold protein A gold in *vha-1(RNAi)* worms (96h)
883 (dark dots). Anti-phospho-ezrin antibody accumulates around *vha-1(RNAi)*-induced vacuole-
884 like structures and on the apical PM. (I) *snap-29(RNAi)* (96h) also induced the formation of
885 cytoplasmic ERM-1::mNG$^+$ MVIs. Lower panel is a magnified picture of the MVI indicated
886 by the arrowhead. L, lumen; mv, microvilli; tw, terminal web; AP, apical PM; BS, basal PM.
887 Scale bar is shown on each panel.

888

888

889 **Figure 8. Dynamics of microvillus inclusions in *C. elegans***

890 (A) MVIs cytoplasmic nucleation observed by timelapse imaging in endogenous ERM-
891 1::mNG expressing worms silenced for *vha-1* during 96h. Snapshots are shown every 5 min,
892 MVI is indicated by the arrow. (B) MVIs can arise by internalization of the apical or
893 basolateral PM. ERM-1::GFP expressing worms were silenced for *vha-1* during 72h and
894 imaged by conventional (left panel) or super-resolution (right panel) microscopy. Arrowhead
895 and arrow show the apical and basolateral PM, respectively. (C) Irregular MVIs/vacuoles
896 (arrow) are often in the vicinity of lysosomes/mixed-organelles (arrowhead). N2 worms were
897 silenced for *vha-1* during 96h and analyzed by TEM. (D) ERM-1::wSc and LMP-1::GFP
898 colocalize at *vha-1(RNAi)*-induced MVIs (96h). (E-F) 96h *vha-1(RNAi)*-induced MVIs can be
899 surrounded by a second ERM-1^{+} layer in which MVIs are degraded. (E) shows a super-
900 resolution image of an MVI (arrowhead) and the surrounding ERM-1^{+} layer (arrow), (F)
901 shows a timelapse imaging of *vha-1(RNAi)*-induced MVI disappearance (image every 4 min).
902 (G-H) Autophagy is activated more upon *vha-1(RNAi)* than *vha-8(RNAi)*. LGG-1::GFP
903 expressing worms were silenced for *vha-1* or *vha-8* during 72h and imaged. (H) shows the
904 quantification of LGG-1::GFP apical/cytoplasmic (Ap/cyto) ratio. Histograms are mean ±
905 SEM on each panel, dots represent individual worms and the total number of worms from 3
906 independent experiments is indicated in brackets. ****$p<0.0001$.

907

907 **Supporting information**

908

909 **Fig S1. V0-ATPase silencing affects the polarized localization of polarity modules and**
910 **brush border components.** (A) Polarity screen results. GFP::CDC-42 (upper panels) and
911 ERM-1::GFP (lower panels) expressing strains were silenced for control (L4440), V0-
912 ATPase (*vha-1*) or V1-ATPase (*vha-8*) specific RNAi during 72h and imaged. Note the
913 basolateral accumulation of both markers upon *vha-1(RNAi)*. (B-C) Effect of 72h *vha-*
914 *1(RNAi)* on the expression of the V0-ATPase subunit VHA-6::mCh. (B) shows representative
915 images and (C) the quantification of VHA-6::mCh apical/cytoplasmic ratio. The histogram
916 shows the mean ± SEM, dots represent individual worms and the total number of worms from
917 3 independent experiments is indicated in brackets. ****p<0.0001. (D) 72h *vha-6(RNAi)* also
918 induces a basolateral mislocalization of ERM-1::GFP (arrowheads). Arrows and arrowheads
919 show the apical and basolateral PM, respectively.

920 **Fig S2. V0-ATPase polarity maintenance pathway.** (A) Effect of 72h V0- or V1-ATPase
921 silencing on the basolateral/cytoplasmic (Bl/cyto) ratio of SLCF-1. Left panel shows a
922 representative experiment. (B) Both *vha-1* and *vha-8(RNAi)* (72h) induce an accumulation of
923 GFP::RAB-7 and GFP::RAB-10 in large cytoplasmic structures. Image shown is
924 representative of 52-66 RAB-7::GFP and 38-58 RAB-10::GFP expressing worms observed
925 for each condition, out of 3-5 independent experiments. (C) Effect of 72h V0- or V1-ATPase
926 silencing on the basolateral/cytoplasmic (Bl/cyto) ratio of SYX-1/SYN-1. Left panel shows a
927 representative experiment. (D-F) *snap-29(RNAi)* decreases SNAP-29::GFP expression and
928 CDC-42::GFP apical localization. (E) represents the apical/cytoplasmic ratio of SNAP-
929 29::GFP. (G-H) *rab-11(RNAi)* decreases RAB-11 expression. (H) shows the quantification of
930 RAB-11::GFP apical/cytoplasmic ratio. Histograms are mean ± SEM on each panel, dots

931 represent individual worms and the total number of worms from 3 (A, C) or 1 (E, F)
932 experiment(s) is indicated in brackets. n.s. non-significant, ***p<0,001, ****p<0,0001.
933
934 **Fig S3. Ultrastructural analysis of V0-ATPase depletion associated defects.** (A) V0- or
935 V1-ATPase subunits silencing affects *C. elegans* development. Histogram shows the
936 measurement of the worms' diameter from TEM images. (B) *vha-1* silencing often induced a
937 detachment of the PM from the terminal web as well as (C-D) increased the length of cell
938 junctions (CeAJ). (D) shows the measurement of the electron-dense cell-cell junction length
939 on TEM pictures. (E) *vha-1* depleted worms accumulate cell and/or bacterial debris in the
940 intestinal lumen. (F) *vha-1* depleted N2 worms, contrary to control or *vha-8*-depleted worms,
941 are devoid of yolk storage granules (arrows). L, lumen; mv, microvilli; tw, terminal web; AP,
942 apical PM; BS, basal PM; CeAJ, *C. elegans* adherens junctions. Histograms show the mean ±
943 SEM, dots represent individual worms and the total number of worms is indicated in
944 brackets. n.s. non-significant, ****p<0,0001.
945
946 **Fig S4. MVIs onset by internalization of the apical PM.** 3D projection of ERM-1::GFP
947 expressing worms silenced for *vha-1* during 72h. The arrow indicates the internalization of
948 the apical PM. Note the large hole induced by the PM invagination (arrowhead). Scale bar: 5
949 μm.
950
951 **Fig S5. Comparison of polarity maintenance pathways.** In control cells, AP-1, Clathrin
952 and GSLs ensure the correct sorting of polarity and brush border proteins, directly or through
953 adaptor proteins, to the apical PM. PM targeting likely involves RAB-11^{+} apical recycling
954 endosomes, from which polarity/brush border/adaptors-containing vesicles fuse with the PM
955 in a V0-ATPase/Myo5B/STX3/Munc18-2-dependent manner. Upon AP-1 and/or Clathrin

956 and/or GSLs depletion, the early apical sorting step is defective, leading to a polarity
957 inversion that induces the lateral accumulation of apical factors and the formation of lateraly
958 positionned ectopic apical membranes. Upon V0-ATPase or Myo5B/STX3/Munc18-2
959 depletion, a late apical exocytosis step is defective, which affects only trafficking (i.e. SNAP-
960 29 or STX3) and induces the misrouting of polarity/brush border components to the
961 basolateral PM or in MVIs.
962
963 **Table S1. Polarity maintenance screen results.** White and blue cases indicate the genes that
964 affect CDC-42 only or CDC-42 and ERM-1 apical localization, respectively.
965 **Table S2. Comparison of *vha-1* and *vha-8* silencing phenotypes.**
966 **Table S3. Comparison of MVID and V0-ATPase depletion phenotypes.** Adapted from
967 (49), with minor modifications.
968 **Table S4. *C. elegans* strains used in this study.**
969 **Movie S1. Cytoplasmic nucleation of MVIs.** Maximum projection of ERM-1::mNG
970 expressing worms silenced for *vha-1* during 96h. Arrows indicate nucleating MVIs.
971 **Movie S2. Cytoplasmic nucleation of MVIs.** Maximum projection of ERM-1::mNG
972 expressing worms silenced for *vha-1* during 96h. Arrowheads and arrows indicate irregular
973 MVIs/vacuoles and cytoplasmic nucleating MVIs, respectively.
974 **Movie S3. MVI formation by internalization of the apical PM.** 3D projection of ERM-
975 1::GFP expressing worms silenced for *vha-1* during 72h.
976 **Movie S4. MVI elimination.** Maximum projection of ERM-1::mNG expressing worms
977 silenced for *vha-1* during 96h. The arrow indicates the elimination of the MVIs inside the
978 presumptive autophagic ERM-1^{+} membrane. Arrowheads show direct MVI disappearance in
979 the cytoplasm.

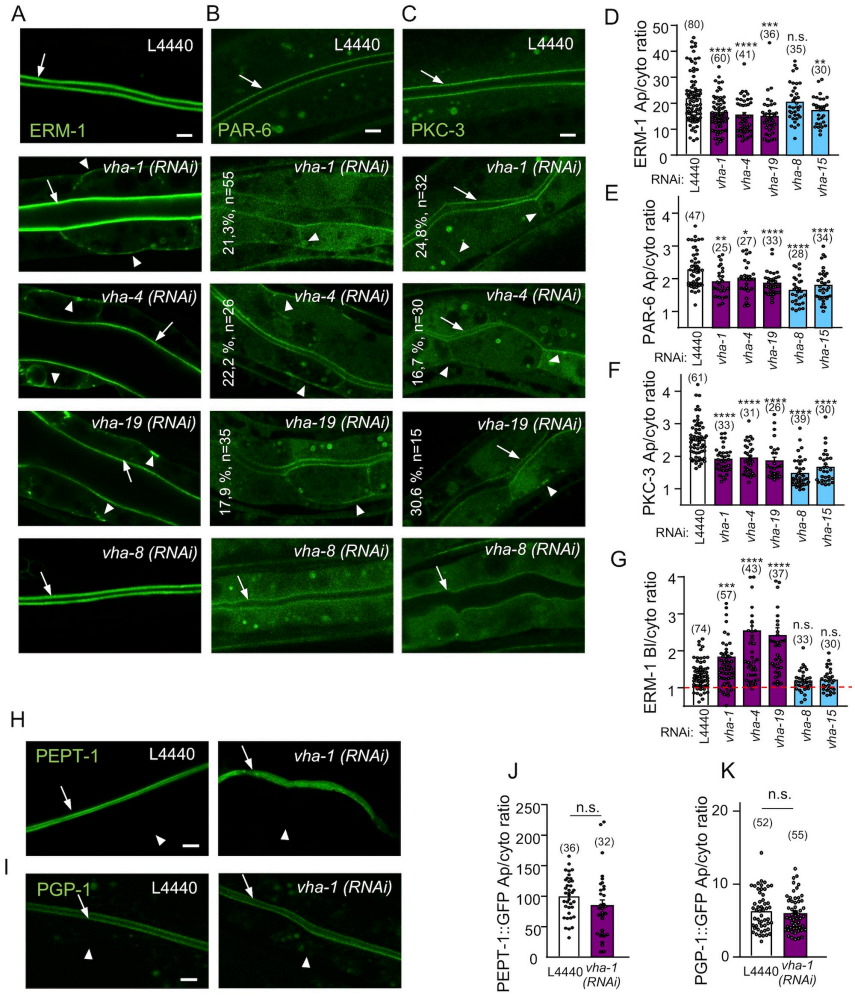
A
B
C
L4440
ERM-1
PAR-6
PKC-3
vha-1 (RNAi)
vha-4 (RNAi)
vha-19 (RNAi)
vha-8 (RNAi)
21,3%, n=55
24,8%, n=32
22,2 %, n=26
16,7 %, n=30
17,9 %, n=35
30,6 %, n=15
D
ERM-1 Ap/cyto ratio
E
PAR-6 Ap/cyto ratio
F
PKC-3 Ap/cyto ratio
G
ERM-1 Bl/cyto ratio
RNAi:
L4440
vha-1
vha-4
vha-19
vha-8
vha-15
n.s.
H
PEPT-1
I
PGP-1
J
PEPT-1::GFP Ap/cyto ratio
K
PGP-1::GFP Ap/cyto ratio
vha-1 (RNAi)

Figure 1

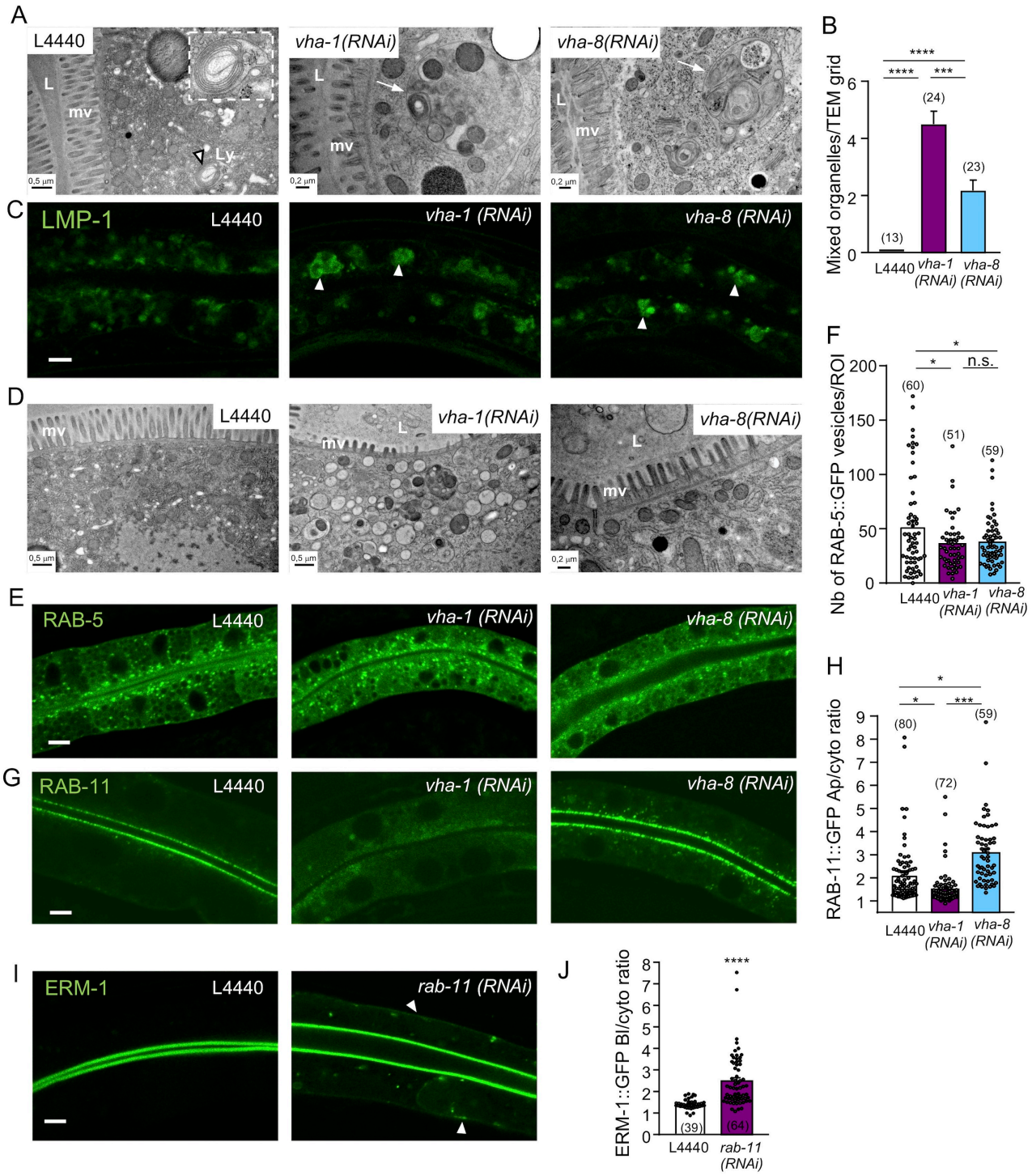
A
L4440
vha-1(RNAi)
vha-8(RNAi)
L
mv
Ly
0,5 µm
0,2 µm
B
Mixed organelles/TEM grid
****
***
(13)
(24)
(23)
L4440
vha-1 (RNAi)
vha-8 (RNAi)
C
LMP-1
L4440
vha-1 (RNAi)
vha-8 (RNAi)
D
L4440
vha-1(RNAi)
vha-8(RNAi)
F
Nb of RAB-5::GFP vesicles/ROI
*
n.s.
(60)
(51)
(59)
E
RAB-5
L4440
vha-1 (RNAi)
vha-8 (RNAi)
G
RAB-11
L4440
vha-1 (RNAi)
vha-8 (RNAi)
H
RAB-11::GFP Ap/cyto ratio
***
(80)
(72)
(59)
I
ERM-1
L4440
rab-11 (RNAi)
J
ERM-1::GFP BI/cyto ratio
(39)
(64)
L4440
rab-11 (RNAi)

Figure 2

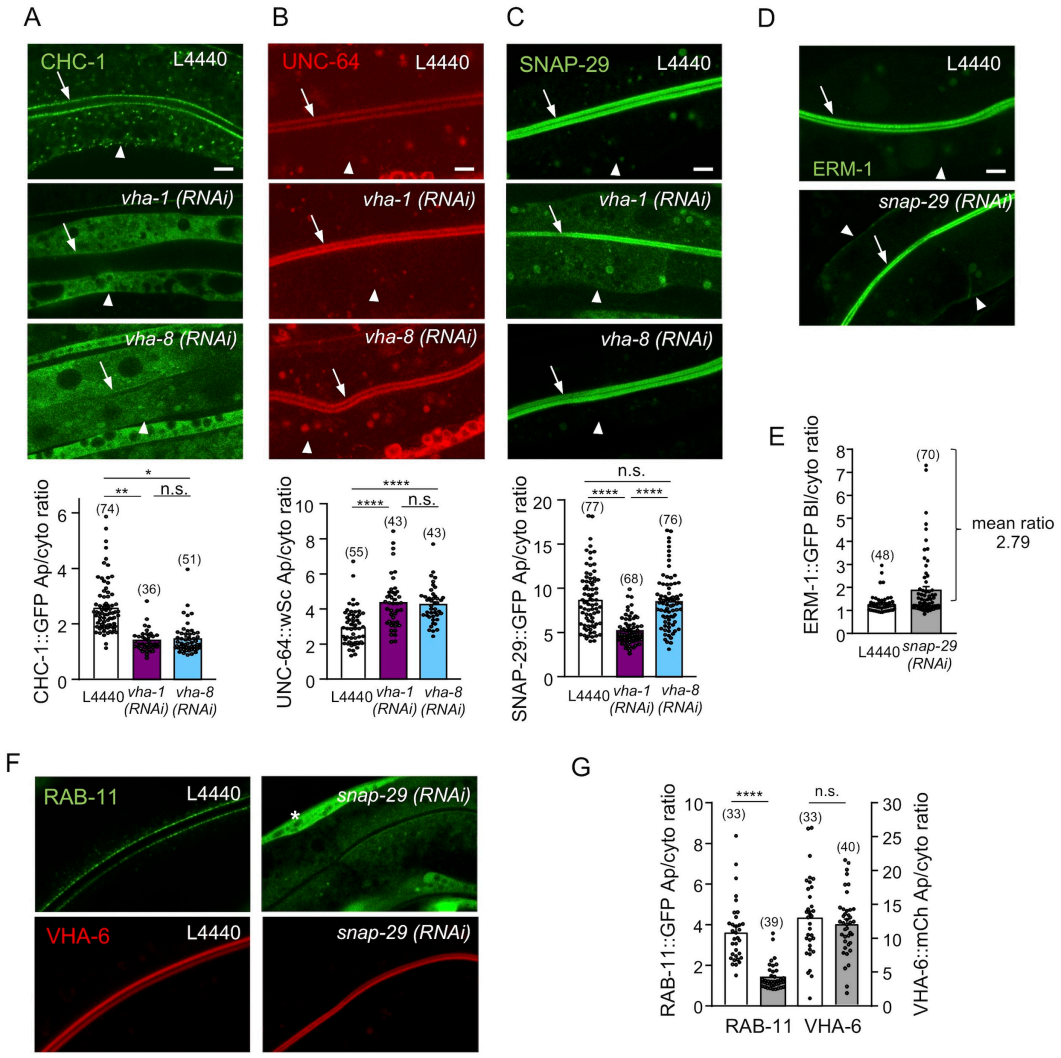
A
CHC-1
L4440
vha-1 (RNAi)
vha-8 (RNAi)
CHC-1::GFP Ap/cyto ratio
B
UNC-64
L4440
vha-1 (RNAi)
vha-8 (RNAi)
UNC-64::wSc Ap/cyto ratio
C
SNAP-29
L4440
vha-1 (RNAi)
vha-8 (RNAi)
SNAP-29::GFP Ap/cyto ratio
D
L4440
ERM-1
snap-29 (RNAi)
E
ERM-1::GFP Bl/cyto ratio
mean ratio
2.79
F
RAB-11
L4440
snap-29 (RNAi)
VHA-6
L4440
snap-29 (RNAi)
G
RAB-11::GFP Ap/cyto ratio
VHA-6::mCh Ap/cyto ratio
RAB-11
VHA-6

Figure 3

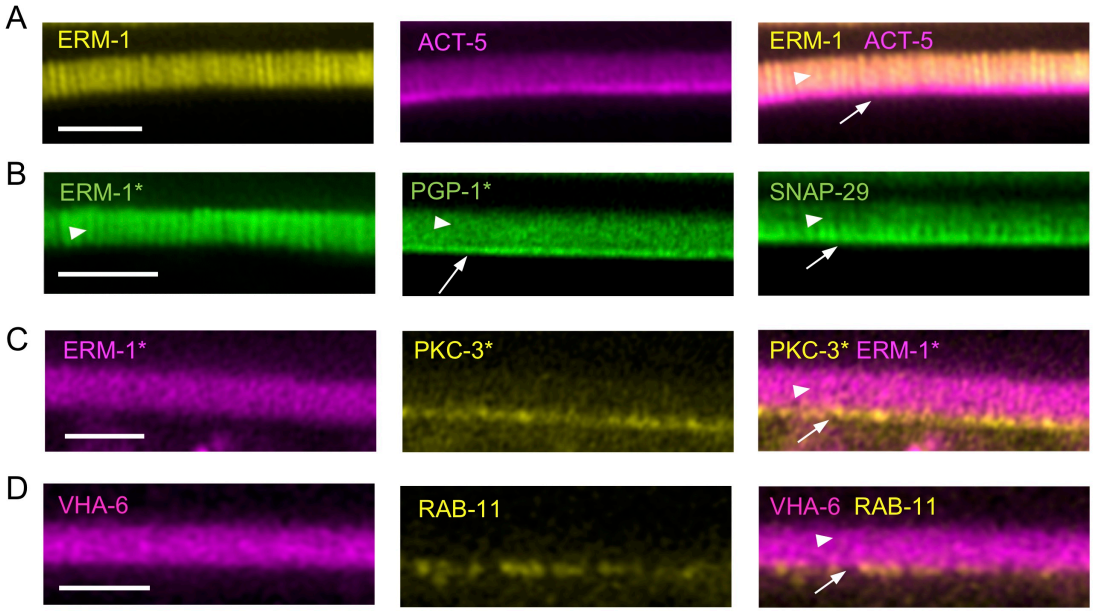
A
ERM-1
ACT-5
ERM-1 ACT-5
B
ERM-1*
PGP-1*
SNAP-29
C
ERM-1*
PKC-3*
PKC-3* ERM-1*
D
VHA-6
RAB-11
VHA-6 RAB-11

Figure 4

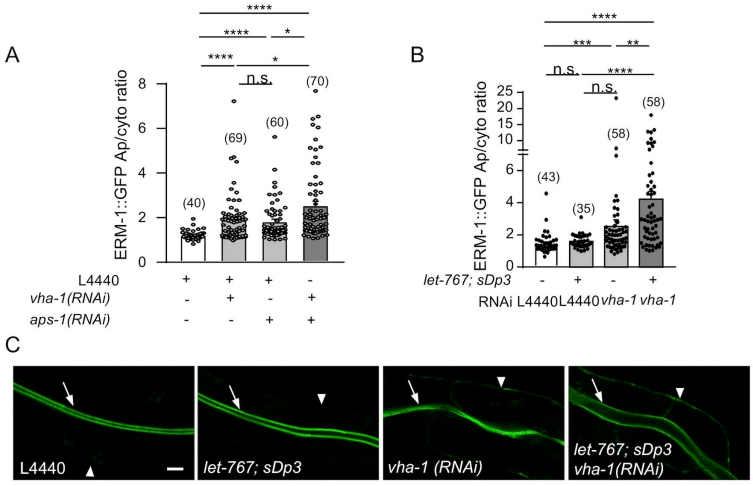
A
B
C
ERM-1::GFP Ap/cyto ratio
L4440
vha-1(RNAi)
aps-1(RNAi)
let-767; sDp3
RNAi L4440 L4440 vha-1 vha-1
n.s.
****
***
**
*
(40)
(69)
(60)
(70)
(43)
(35)
(58)
(58)
L4440
let-767; sDp3
vha-1 (RNAi)
let-767; sDp3
vha-1(RNAi)

Figure 5

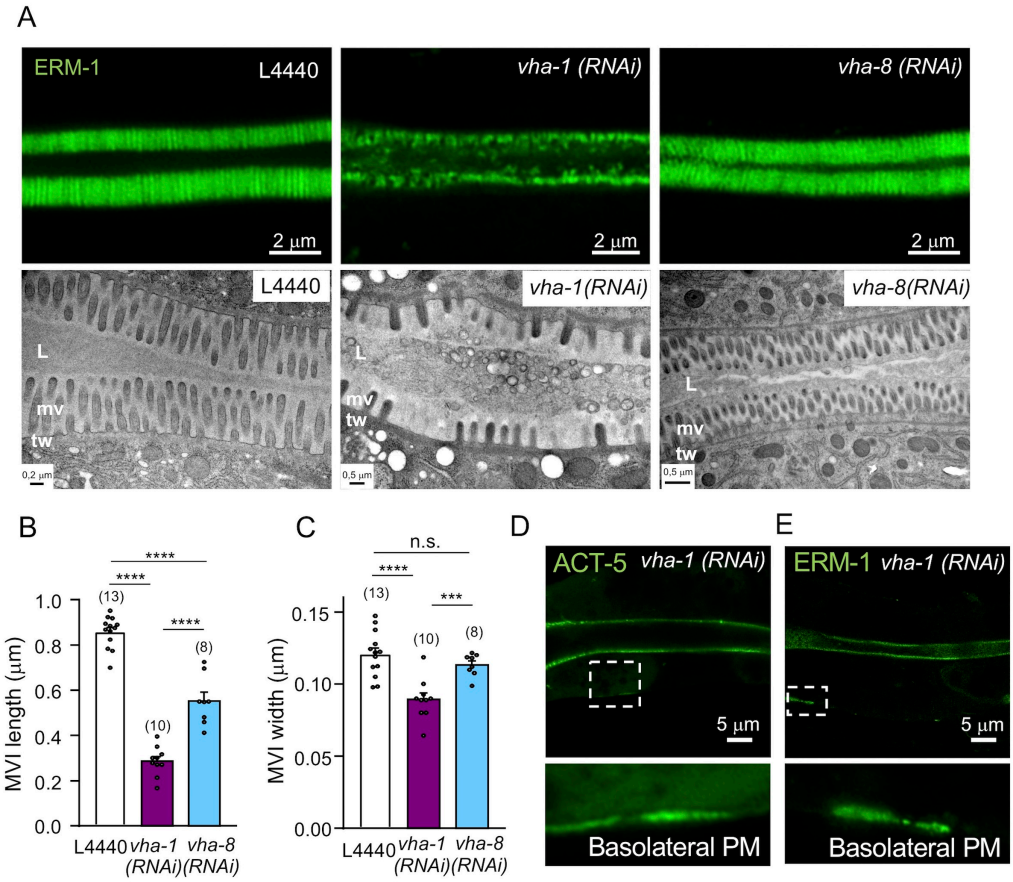
A
ERM-1
L4440
vha-1 (RNAi)
vha-8 (RNAi)
2 µm
L
mv
tw
vha-1(RNAi)
vha-8(RNAi)
B
MVI length (µm)
1.0
0.8
0.6
0.4
0.2
0.0
(13)
(10)
(8)
****
L4440
vha-1 (RNAi)
vha-8 (RNAi)
C
MVI width (µm)
0.15
0.10
0.05
0.00
n.s.
***
D
ACT-5
5 µm
Basolateral PM
E
ERM-1

Figure 6

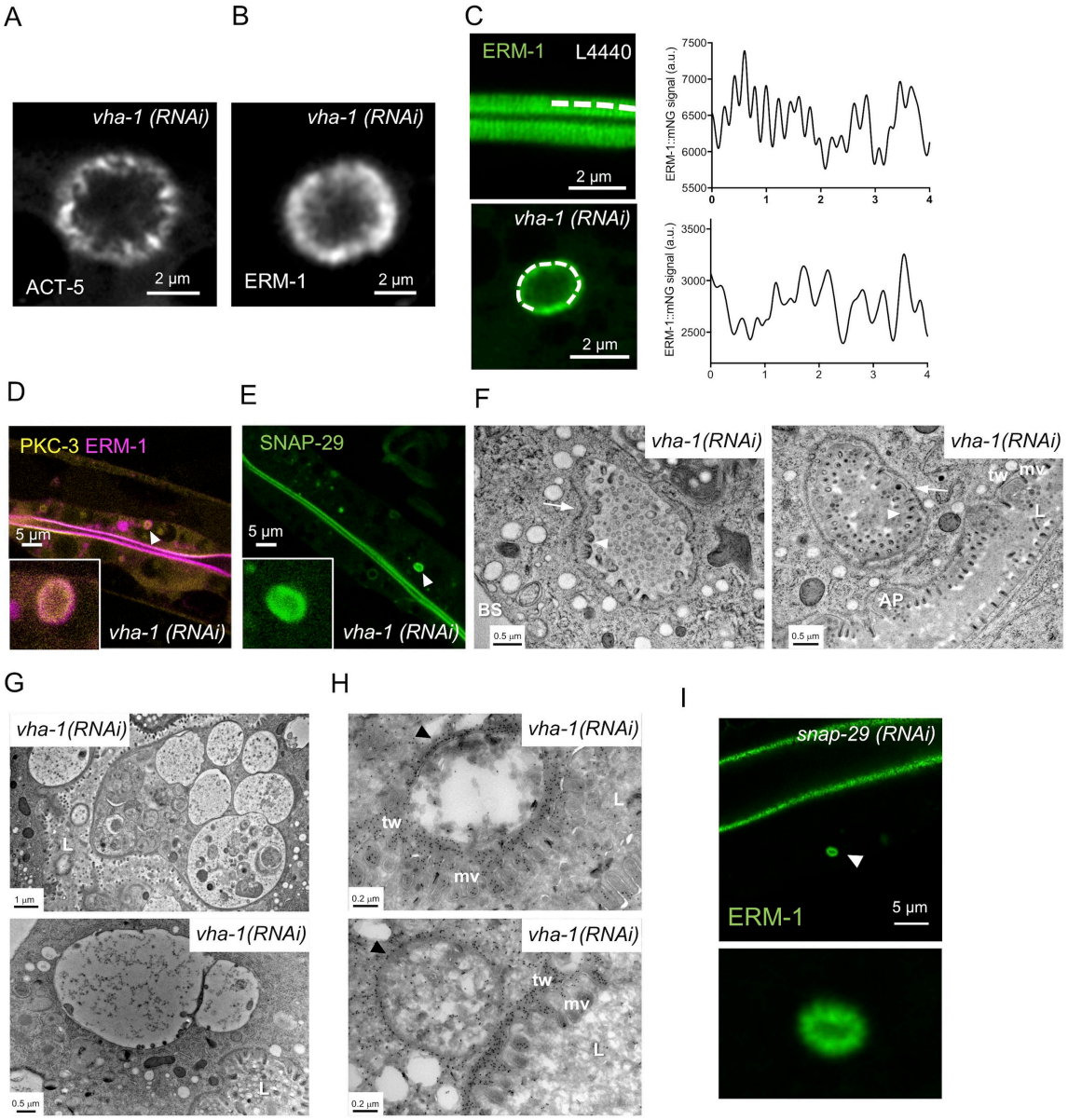
A
vha-1 (RNAi)
ACT-5
2 µm
B
vha-1 (RNAi)
ERM-1
2 µm
C
ERM-1
L4440
2 µm
vha-1 (RNAi)
2 µm
ERM-1::mNG signal (a.u.)
7500
7000
6500
6000
5500
0
1
2
3
4
ERM-1::mNG signal (a.u.)
3500
3000
2500
0
1
2
3
4
D
PKC-3 ERM-1
5 µm
vha-1 (RNAi)
E
SNAP-29
5 µm
vha-1 (RNAi)
F
vha-1(RNAi)
BS
0.5 µm
vha-1(RNAi)
tw
mv
L
AP
0.5 µm
G
vha-1(RNAi)
L
1 µm
vha-1(RNAi)
L
0.5 µm
H
vha-1(RNAi)
tw
L
mv
0.2 µm
vha-1(RNAi)
tw
mv
L
0.2 µm
I
snap-29 (RNAi)
ERM-1
5 µm

Figure 7

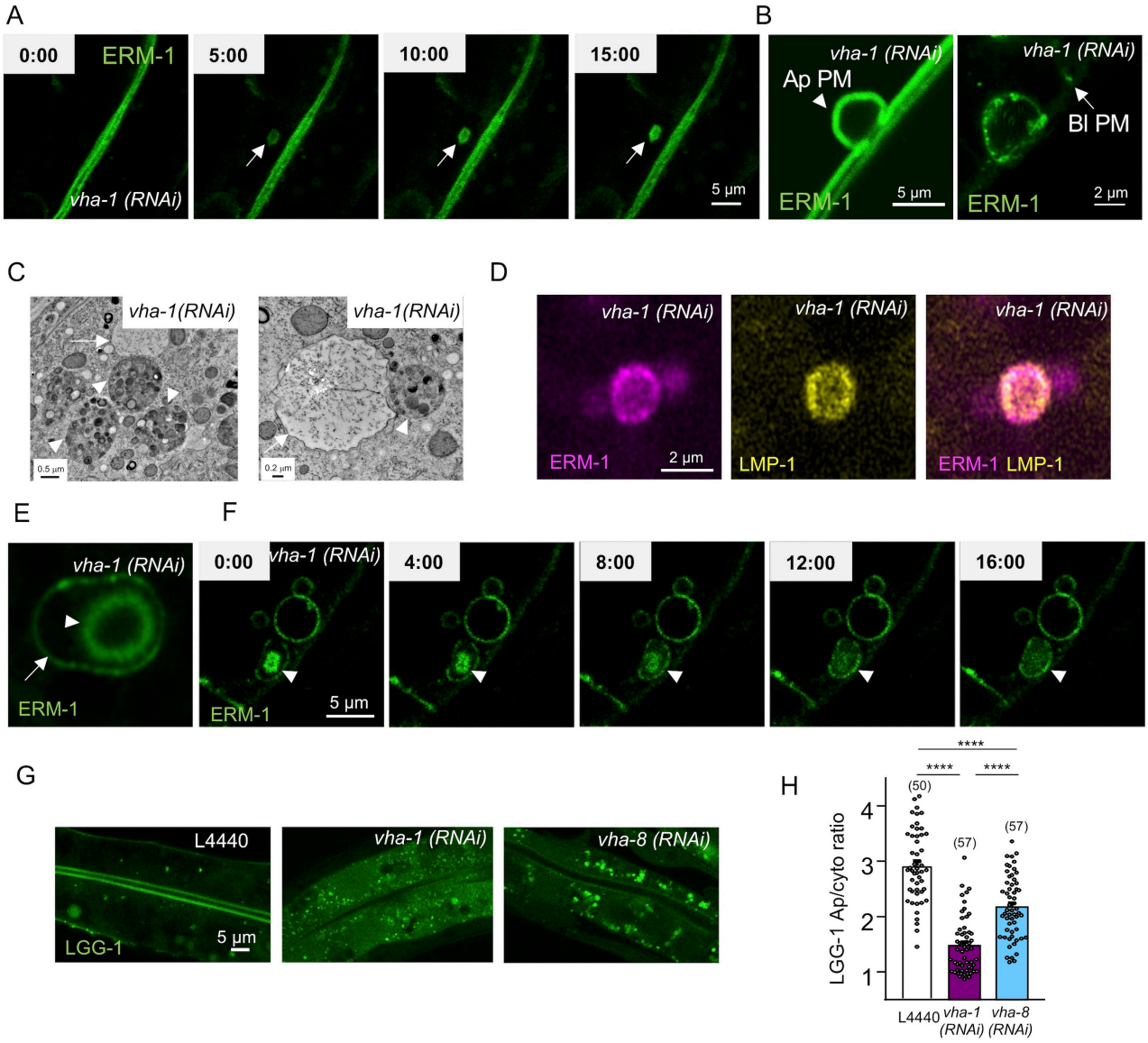
A
0:00
ERM-1
vha-1 (RNAi)
5:00
10:00
15:00
5 µm
B
vha-1 (RNAi)
Ap PM
ERM-1
5 µm
vha-1 (RNAi)
Bl PM
ERM-1
2 µm
C
vha-1(RNAi)
vha-1(RNAi)
D
vha-1 (RNAi)
ERM-1
2 µm
vha-1 (RNAi)
LMP-1
vha-1 (RNAi)
ERM-1 LMP-1
E
vha-1 (RNAi)
ERM-1
F
0:00
vha-1 (RNAi)
ERM-1
5 µm
4:00
8:00
12:00
16:00
G
L4440
LGG-1
5 µm
vha-1 (RNAi)
vha-8 (RNAi)
H
****
****
****
(50)
(57)
(57)
LGG-1 Ap/cyto ratio
4
3
2
1
L4440
vha-1 (RNAi)
vha-8 (RNAi)

Figure 8

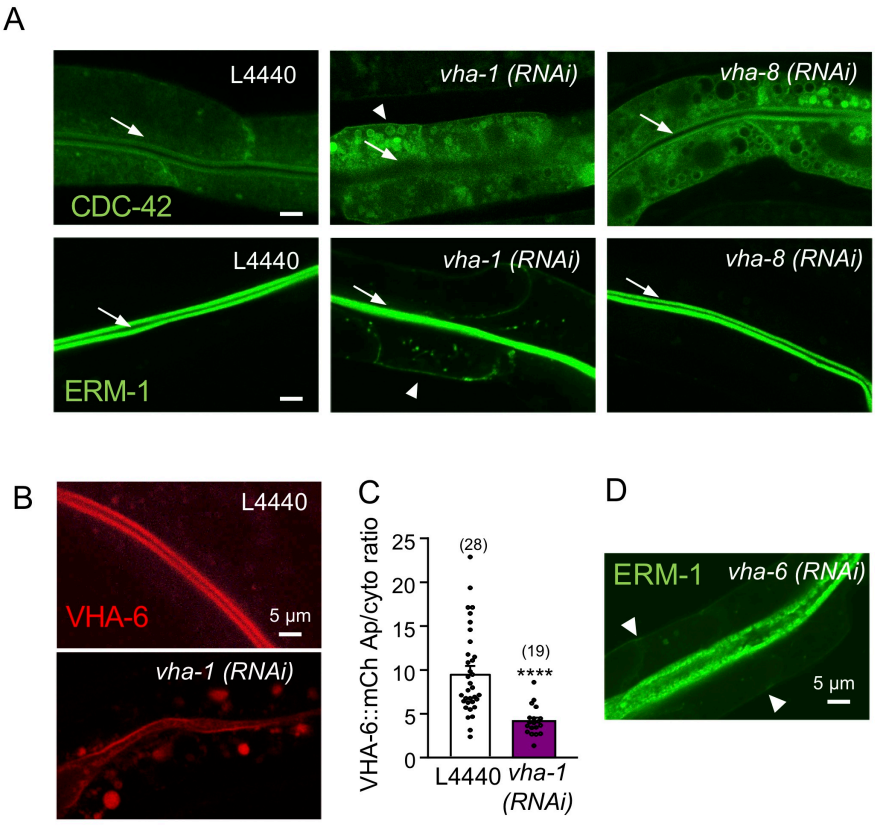
A
L4440
vha-1 (RNAi)
vha-8 (RNAi)
CDC-42
L4440
vha-1 (RNAi)
vha-8 (RNAi)
ERM-1
B
L4440
VHA-6
5 µm
vha-1 (RNAi)
C
VHA-6::mCh Ap/cyto ratio
25
20
15
10
5
0
(28)
(19)
****
L4440
vha-1 (RNAi)
D
ERM-1
vha-6 (RNAi)
5 µm

Figure S1

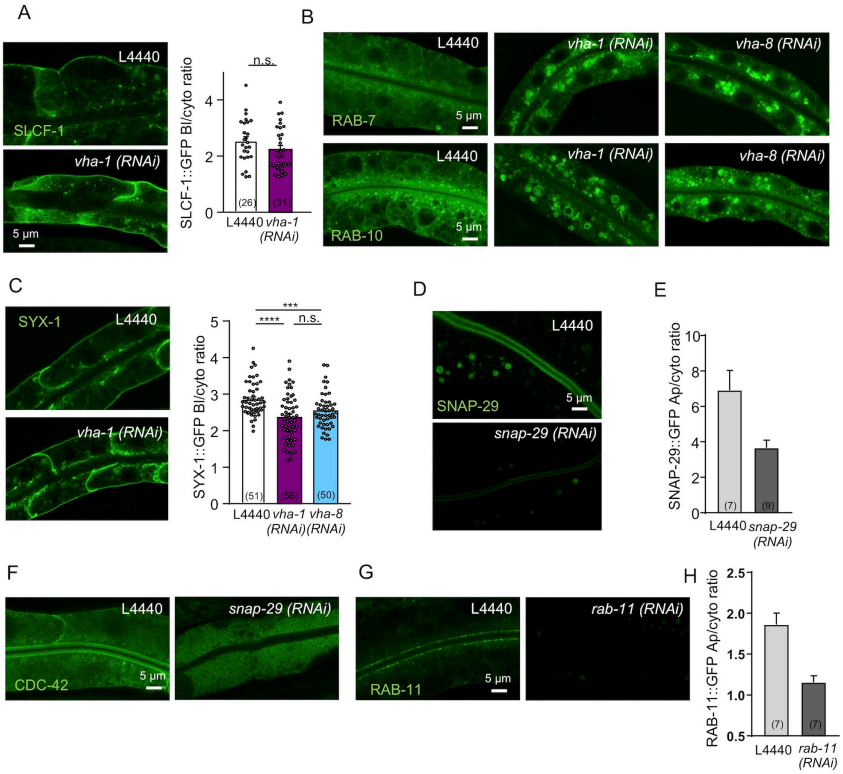
A
L4440
SLCF-1
vha-1 (RNAi)
5 µm
n.s.
SLCF-1::GFP Bl/cyto ratio
(26)
(31)
L4440
vha-1 (RNAi)
B
L4440
RAB-7
5 µm
vha-1 (RNAi)
vha-8 (RNAi)
L4440
RAB-10
5 µm
vha-1 (RNAi)
vha-8 (RNAi)
C
SYX-1
L4440
vha-1 (RNAi)
***
****
n.s.
SYX-1::GFP Bl/cyto ratio
(51)
(56)
(50)
L4440
vha-1 (RNAi)
vha-8 (RNAi)
D
L4440
SNAP-29
5 µm
snap-29 (RNAi)
E
SNAP-29::GFP Ap/cyto ratio
(7)
(9)
L4440
snap-29 (RNAi)
F
L4440
CDC-42
5 µm
snap-29 (RNAi)
G
L4440
RAB-11
5 µm
rab-11 (RNAi)
H
RAB-11::GFP Ap/cyto ratio
(7)
(7)
L4440
rab-11 (RNAi)

Figure S2

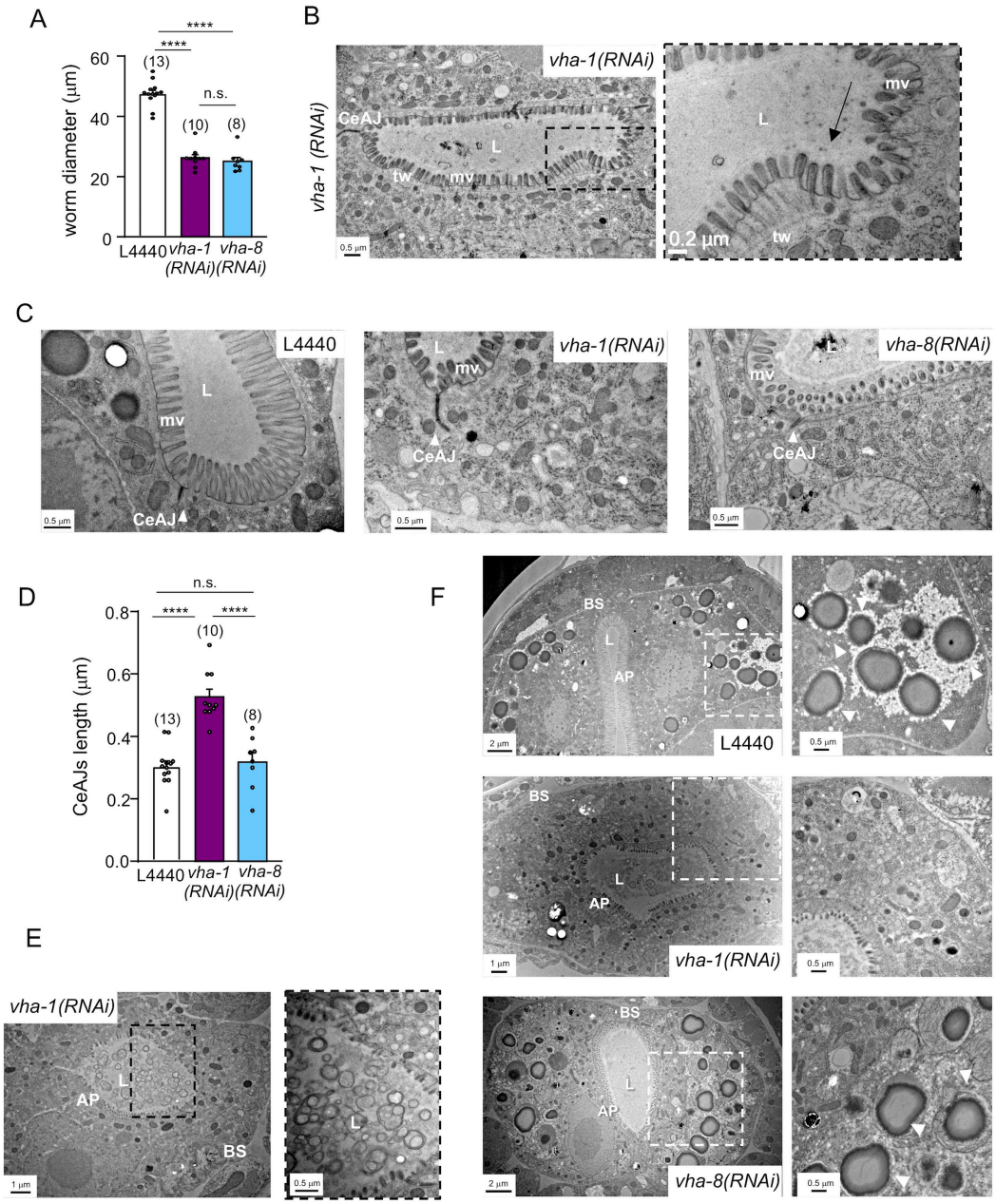
A
****
****
n.s.
(13)
(10)
(8)
worm diameter (µm)
60
40
20
0
L4440
vha-1 (RNAi)
vha-8 (RNAi)
B
vha-1 (RNAi)
vha-1(RNAi)
CeAJ
L
tw
mv
0.5 µm
0.2 µm
C
L4440
vha-1(RNAi)
vha-8(RNAi)
D
n.s.
****
****
(13)
(10)
(8)
CeAJs length (µm)
0.8
0.6
0.4
0.2
0.0
E
F
BS
AP
1 µm
2 µm

Figure S3

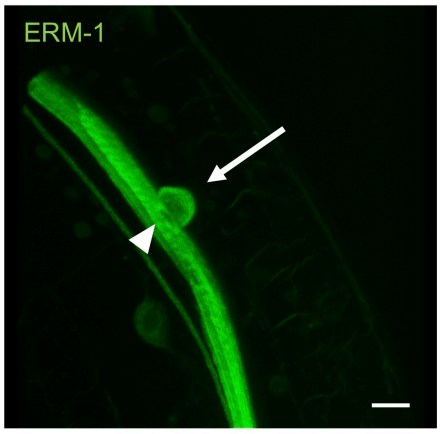

Figure S4

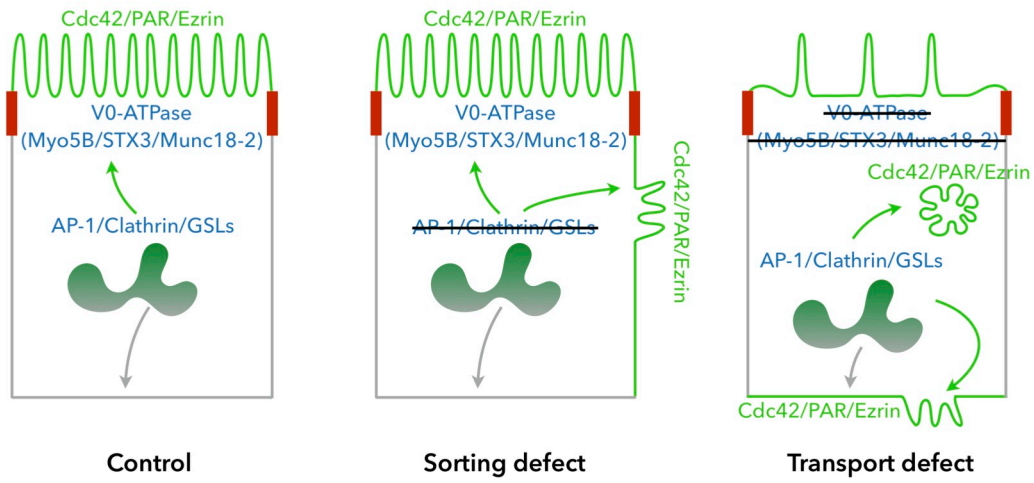
Cdc42/PAR/Ezrin
V0-ATPase
(Myo5B/STX3/Munc18-2)
AP-1/Clathrin/GSLs
Control
Cdc42/PAR/Ezrin
V0-ATPase
(Myo5B/STX3/Munc18-2)
AP-1/Clathrin/GSLs
Cdc42/PAR/Ezrin
Sorting defect
V0-ATPase
(Myo5B/STX3/Munc18-2)
Cdc42/PAR/Ezrin
AP-1/Clathrin/GSLs
Cdc42/PAR/Ezrin
Transport defect

Figure S5

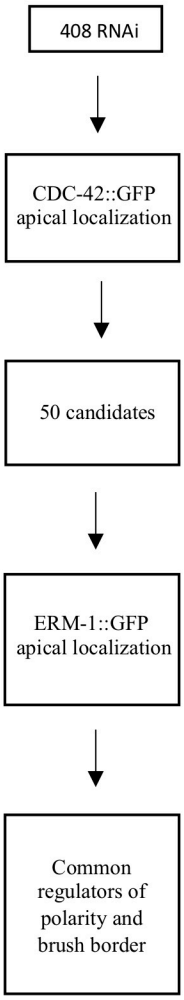

Family	Gene
COPI	E03H4.8
	copb-1
	COPI zeta
	copb-2
Cytoskeleton	act-5
	IFB-1
ECM	noah-1
ER traffic	lpin-1
	sly-1
ESCRTIII	vps-32.1
F ATPase	H28O16.2
GSL	fasn-1
	pod-2
	sptl-1
Membrane fusion	nsf-1
	snap-29
	snap-1
	unc-64
	syx-3
	syx-5
	syx-7
Muscle	let-805
	vab-10
	pat-10
NADPH oxidase	bli-3
Sorting	aps-1
	chc-1
PAR	cdc-42
Rabs	rab-5
Ribosome	rpl-36
V-ATPase	vha-4
	unc-32
	vha-1
	vha-19
	vha-17
	vha-15
	vha-20
	vha-10
	vha-8
	vha-12

Table S1

	L4440	***vha-1(RNAi) (V0)***	***vha-8(RNAi) (V1)***
PAR-6, PKC-3, ERM-1 apical PM	Normal	Down	Down
Basolateral PAR-6, PKC-3, ERM-1	No	Yes	No
SNAP-29 cytoplasmic accumulation	No	Yes	No
Mixed organelles	No	Yes	Yes
LMP-1, RAB-7, RAB-10 accumulation	No	Yes	Yes
Autophagy activation	No	+++	+
Accumulation of cytoplasmic lucent vesicles	No	Yes	No
RAB-11 signal	-	Down	Up
Microvillus atrophy	No	Yes	No
MVIs, vacuoles	No	Yes	No

Table S2

MVID phenotype	Normal intestine	*MYO5B* deficient patients	*STX3* deficient patients	*MUNC18-2* deficient patients (FHL5)	*MUNC18-2* $^{-/-}$ mouse organoids	*vha-1* RNAi *C. elegans*
microvillus atrophy (absent or abnormal microvilli)	no	yes	yes	yes	yes	yes (Fig 4)
microvillus inclusions	no	frequent, observed in 10% of cells	infrequent	infrequent, not fully penetrant	frequent but only after differentiation	infrequent (Fig 5)
basolateral microvilli	no	incomplete penetrance	frequent	frequent	frequent but only after differentiation	probable (Fig 5)
vesicle or tubulo-vesicular structures accumulation	no	Apical vesicles and tubulovesicular; variable electron-dense and translucent	Apical vesicles and tubulovesicular; variable electron-dense and translucent (villus)	electron-dense and translucent apical vesicles	crypt: translucent apical villus: translucent tubulovesicular apical	endosome like vesicles and enlarged vacuolar structures (Fig 2)
RAB-11+ apical recycling endosomes loss	no	yes	yes	yes	yes	yes (Fig 2)
lysosomal abnormalities	no	Enlarged (auto)lysosomes	Enlarged (auto)lysosomes	high number of lysosomes	enlarged lysosomes	enlarged and high number of lysosomes (Fig 2)
STX3 localization	apical membrane	Subapical vesicle and MVIs	reduced/absentprote in level	subapical vesicle and MVIs	diffuse in cytoplasm	UNC-64 (STX3 ortholog) membrane accumulation (Fig 3)
Brush border proteins defects (ERM-1, ACT-5)	strong in brush border	Reduced brush border signal, MVIs positive	presence of dot- and ring-like structures	reduced brush border, MVIs stained; variable penetrance and severity	reduced brush border, cytoplasmic foci and MVIs stained	reduced brush border, presence of MVI structures (Fig 1, 4, 5, 6)

Table S3

Srain name	Genotype	Reference
MCP59	*bab59[erm-1::mNG^SEC^3xFlag] I*	This study
MCP64	*erm-1(bab91[erm-1::wrmSc^3xFlag]) I*	This study
FL369	*fgEx13[perm-1::erm-1::gfp + rol-6 (su1006)] ; jyIs17 [vha-6p::mcherry::act-5, ttx-3p::RFP]*	This study
FL316	*dfEx3 [vha-6p::gfp::cdc-42 + rol-6 (su1006)]; unc-119(ed3)III; mcls46 [dlg-1::rfp+unc-119(+)]*	This study
KK1248	*par-6(it319[par-6::GFP]) I*	CGC
KK1228	*pkc-3(it309[GFP::pkc-3]) II*	CGC
GK446	*unc-119(ed3) ; dkIs259[Pact-5-GFP-snap-29 ; Cb.unc-119(+)]*	Sato et al., 2011
FL373	*pkc-3(it309[GFP::pkc-3]) II; erm-1(bab91[erm-1::wrmSc^3xFlag]) I*	This study
MCP111	*bab113[mNG^3xFlag::pgp-1] IV*	This study
KWN117	*rnyEx60 [pELA2 (vha-6p:::vha-6::mCherry) + myo-3p::GFP + pCL1 (pha-1+)]*	V. Gobel
FL375	*rnyEx60 [pELA2 (vha-6p:::vha-6::mCherry) + myo-3p::GFP + pCL1 (pha-1+)]; pwIs69 [vha6p::GFP::rab-11 + unc-119(+)]*	This study
KWN246	*pha-1(e2123) III, rnyEx133[opt-2(aa1-412)::GFP) + pha-1(+)]*	CGC
FL368	*bls5[chc-1p::gfp::chc-1 + rol-6(su1006)]; jyls17 [vha-6p::mcherry::act-5, ttx-3p::RFP]*	
MCP91	*unc-64(bab91[wrmSc^3xFlag ::unc-64]) III*	This study
RT258	*pwIs50 [lmp-1::GFP + Cbr-unc-119(+)]*	CGC
RT327	*pwIs72 [vha-6p::GFP::rab-5 + Cbr-unc-119(+)]*	CGC
RT476	*pwIs170 [vha6p::GFP::rab-7 + Cbr-unc-119(+)]*	CGC
RT525	*pwIs206 [vha6p::GFP::rab-10 + Cbr-unc-119(+)]*	CGC
RT311	*pwIs69 [vha6p::GFP::rab-11 + unc-119(+)]*	CGC
VJ268	*fgEx12[pact-5::act-5::gfp]*	Zhang et al., 2012
FL376	*pwIs50 [lmp-1::GFP + Cbr-unc-119(+)]; erm-1(bab91[erm-1::wrmSc^3xFlag]) I*	This study
GK385	*unc-119(ed3) ; dkIs218[Popt-2-GFP-syn-1 ; Cb.unc-119(+)]*	Sato et al., 2011
FS254	*slcf-1(tm2258); Exfs254[slcf-1::gfp]*	Mouchiroud et al., 2010
DA2123	*adIs2122 [lgg-1p::GFP::lgg-1 + rol-6(su1006)]*	CGC
	Rab11 VHA-6	This study
VJ500		

Table S4